4-4-2022

Effects of Varied Oxygen Levels, Laser Powers, and Scanning Speeds on Manufactured Components by Laser-Based Powder Bed Fusion

Amelia McNamee
Georgia Southern University

Effects of Varied Oxygen Levels, Laser Powers, and Scanning Speeds on Manufactured Components by Laser-Based Powder Bed Fusion

An Honors Thesis submitted in partial fulfillment of the requirements for Honors in Mechanical Engineering.

By
Amelia McNamee

Under the mentorship of Dr. Drew Snelling

ABSTRACT

This project addresses the effects of oxygen concentration, laser power, and scanning speed on the melt pool geometry of laser-based powder bed fusion (L-PBF) additively manufactured components. A parametric analysis using the substrate alone was conducted to determine a range of desirable laser powers and scanning speeds. The parameter with the more significant effect will be decided upon based on the depth-to-width ratios (D/W) of the resultant laser weld bead. A range of oxygen levels and scan speeds was selected for the next phase. These samples were then be analyzed for depth-to-width ratios. It was expected that higher oxygen concentrations will result in larger depth-to-width ratios due to the reversal of the Marangoni convection and that lower scan speeds and higher laser powers would yield larger depth-to-width ratios due to increased input energy density. It was determined that increased oxygen levels, up to approximately 1.5% oxygen, slower scanning speeds, with a minimum of approximately 300 mm/s, and higher laser powers yielded increasing D/W ratios. Additionally, the similarity between average and median D/W ratios, along with small standard deviations, indicate that the data exhibits acceptable accuracy and precision.

Thesis Mentor:_____

Dr. Drew Snelling

Honors Director:_____

Dr. Steven Engel

April 2022
Mechanical Engineering
Honors College
Georgia Southern University

Acknowledgements

First and foremost, I want to thank Dr. Snelling for taking on the role of faculty advisor and being my mentor through this honors project. His patience, willingness to work with me and my sometimes-crazy schedule, and overall mentorship have made this thesis possible and a journey full of skills and knowledge gained that can be applied as I continue in my career. Another thanks goes to the Honors College. If it wasn't for research being a requirement, I may not have taken the jump and discovered so many fascinating ways that engineering is being advanced here at Georgia Southern University.

Thank you to the Department of Mechanical Engineering for all the knowledge and care they give their students, and especially to Dr. Vlcek for granting permission to conduct research with a faculty member of the Department of Manufacturing Engineering.

Lastly, thank you to my mom, dad, sister, friends, and those who have been through this experience. Your encouragement, support, love, and prayers helped me complete this project. Thank you for sticking by me, even when the stress drives me a bit crazy.

TABLE OF CONTENTS

NOMENCLATURE

$\%Error$	percent error
D/W	depth-to-width ratio
$depth$	maximum distance from top of substrate to bottom of bead
$experimental$	experimentally determined value
i	number of the term being evaluated
N	number of terms being evaluated
$theoretical$	theoretical or target value
$width$	distance from bead left-hand side to bead right-hand side, maximum
x_i	ith term being evaluated
$\overline{x}$	calculated average value
σ	population standard deviation

LIST OF FIGURES

LIST OF TABLES

1. INTRODUCTION

1.1 Background and Motivation for Research

Additive manufacturing (AM) is used to describe a collection of disruptive technologies that have significantly altered the way many parts are manufactured. Typically, geometrically complex parts would require multiple steps in manufacturing, such as with a multi-axis CNC. Additionally, the manufacture of complex components is traditionally done through subtractive manufacture, which results in material waste due to the material removal and thus unnecessary material costs. AM holds the potential to manufacture such parts in one step, with less material waste, and at a lower cost. Since it is still a relatively new manufacturing technology, there is a significant opportunity for research in order to gain a robust understanding of the processes, parameters, limitations, etc. Some of this knowledge can be estimated from similar processes, such as welding or casting; however, there are areas where AM and the older methods diverge and thus should be tested and experimentally determined. The key differences between more traditional manufacturing processes and novel metal AM are the process scale, energy source, and that the latter requires rapidly melting and re-solidifying the metal. It is these key differences between traditional processes and the newer, less-studied AM methods that prevent the knowledge of existing methods from being fully extrapolated to the novel AM methodology while retaining a high degree of certainty in the quality of the assumptions. Hence, the techniques must be thoroughly investigated, though older methods can be used to develop hypotheses for expected results. Since additive manufacturing holds great promise for future manufacturing, it is imperative that the processes be thoroughly understood so that their future use can be maximized. By characterizing the behavior of the

melt pool with regards to the specified parameters, component features such as the D/W ratio can be better controlled. This understanding of how to control the ratio is imperative in order to produce a desirable ratio based on the application of the part being manufactured as well as mitigate part failure. As beads with either overly large or small D/W ratios are considered more susceptible to stresses during the solidification process, increasing the risk of cracking and failure, it is critical for the melt pool size to be maintained within a range which mitigates such risks. By understanding how the morphology of the bead is affected by laser power, scan speed, and oxygen concentration, the input parameters can be set to produce an ideal bead geometry.

1.2 Literature Review

Because there is limited research studying the effect of oxygen on melt pool geometry for L-PBF, the authors look to similar traditional manufacturing techniques that rely on the influence of shielding gas, for example, welding. Heiple et al (1985) discovered that increasingly lower oxygen levels lowered the D/W ratio of steel beads manufactured via GTAW, with the ratio being as low as 0.15 at an oxygen concentration of 10 ppm [1]. This undesirably shallow weld was well below the typical ratio of 0.5 for D/W [1]. The effect of oxygen concentration in helium and oxygen shielded TIG welding was explored by Fujii et al (2008). The depth-to-width ratio was small for near-non-existent levels of oxygen in the shielding. The ratio then drastically increased with oxygen concentrations from 0.2% to 2.0%, then fell as oxygen concentration in the shielding gas continued to increase [2]. Fujii et al (2006) also investigated how oxygen levels impact TIG welding with an argon-based shielding gas mixture. For oxygen concentrations between 0.3% to 1.0%, the depth-to-width ratio was found to be large, while oxygen levels outside this range produced

drastically lower ratios [3]. Heiple et al (1982) investigated the influence of surface active elements, such as oxygen and selenium, on the fluid flow of GTA weld beads. It was found that increasing amounts of such elements, such as selenium and oxygen, increased the Lorentz force and surface tension gradient such that they induced an inward fluid flow, producing deep and narrow beads [4]. Melt pool morphology resulting from a YAG-TIG combination was analyzed by Naito et al (2006), in which they compared morphologies of beads produced in various gas mixtures. Pure argon yielded melt pools with a "nail head" profile, while increasing amounts of oxygen introduced to the environment yielded deeper and narrow profiles without the "nail head" shape [5]. This was found to be due to the positive surface tension gradient inducing an inward flow of the melt pool [5]. Similar results were found using a CFD analysis and experimental verification of A-TIG welds using 316LN stainless steel, in which oxygen levels at and above 150 ppm produced inward flows [6]. Dong et al (2011) investigated how oxygen concentration and welding parameters influenced the morphology of SUS304 stainless steel manufactured via helium-shielded GTAW. The research was conducted by performing a simulation and establishing a comparison with experimentally determined results [7]. They determined that increasing the presence of oxygen in the shielding gas resulted in deeper, narrower weld cross-sectional profiles due to the direction of the Marangoni convection [7]. Increased welding speeds prevented the development of large temperature gradients and minimized the maximum melt pool temperature, weakening the Marangoni convection and producing shallow, wide welds [7]. Oxygen found in TiO_2 flux for TIG welding was found to have useful effects for the welded steel, as determined by Tathgir et al (2015) [8]. The presence of oxygen increased the absorbed energy density and temperature of the arc, resulting in a

deeper penetration [8]. Additionally, the presence of oxygen is a key determinant in the temperature coefficient of the surface tension of the melt pool [8]. The Marangoni convection reversed to flow inward due to the presence of oxygen, yielding deeper welds [8]. Zacharia et al (1989) established that oxygen behaves as a surface active agent in GTA and laser beam welded 304 stainless steel melt pools [9]. The oxygen alters the surface tension gradient and thus changes the flow direction of the molten bead [9]. This reversal induces an increase in bead depth and width [9]. They also found that, while surface active agents hold a significant role in determining the depth-to-width ratio for weld beads, the temperature distribution has significant influence as well [9].

Matilainen et al (2014) determined that energy density input is a key factor in determining melt pool morphology [10]. As the input energy is increased, the depth-to-width ratio increased accordingly [10]. A reduction in beam current produced decreased widths and depths in Ti-6Al-4V EB welded parts [11]. Lee et al (2017) determined that the width and depth of the bead, as well as the overall D/W ratio, decreased with faster scanning speeds and fixed laser power [12]. Due to the higher speeds, less energy was absorbed by the powder, limiting the melting process to potentially incomplete levels [12]. Dilip et al (2017) focused on the influence of process parameters on the morphology of SLM manufactured Ti-Al6-4V alloy components. Both high and low energy input densities yielded component porosities [13]. High energy density resulted in keyhole effects, which in turn introduced porosities to the part [13]. Low energy density insufficiently melted the powder, producing irregular topology [13]. Additionally, low energy density produced narrow melt pool width and led to balling of the molten metal [13]. STS 316/Fe were manufactured using direct energy deposition in order to determine a correlation between

part properties and the input parametric conditions by Nam et al (2018). It was determined that increased laser powers increased both depth and width, but with a more pronounced effect on the bead height [14]. By contrast, increased scan speeds were found to result in decreased bead ratios [14]. The relation of faster scanning speeds producing lower depth-to-width ratios was confirmed for SS409L welds made using GMAW by Gupta et al (2019) [15]. Scime and Beuth (2019) found that the melt pool depth had significant variability for combinations of high laser power and slow scanning speed [16]. Excepting a limited quantity of outliers, the melt pool geometries tended towards a normal distribution for the various process parameter combinations, indicating that specific parametric combinations will generally produce specific results [16]. Thus, melt pool morphology is strongly influenced by input parameters. Narra (2017) used process maps to determine how absorbed power and scanning speed correlated to bead area, width, and depth using a IN718 substrate without powder [17]. Keyholing was determined to occur for depth-to-half-width ratios of 1, or a D/W ratio of 2, while insufficient fusion was identified as depths less than the powder thickness [17]. Both keyholing and insufficient fusion introduced an increased risk of porosities within the bead and were used to evaluate process parameters [17]. In order to produce larger geometries at different powers and speeds, speed variations were within 400 mm/s, while absorbed power variations were within 40 W [17]. As the geometry was reduced, the speed variation increased to 1200 mm/s, while the absorbed power varied by only 45 W [17]. The process maps also illustrated that increasing the amount of power absorbed yielded increases in geometry for constant scanning speeds [17]. Experimental data supported this, as the experimental widths increased as the beam power was increased. Additionally, increases in scanning speed at fixed beam powers produced narrower bead

widths [17]. The experimental bead depths and cross-sectional areas were found to relate directly with beam power and inversely with scanning speed, similar to the bead widths [17]. Specific depth-to-width ratios were then correlated to beam power and scanning speed [17]. To maintain a constant ratio, travel velocity varied significantly as compared to beam power. However, once a critical point was reached for each ratio, the change in beam power began to have a more significant effect on the depth-to-width ratios [17].

It can be seen from the existing literature that great strides have been made to understand the process of novel metal additive manufacturing methods. Mechanically desirable D/W ratios have been found to range from the typical value of about 0.5 [1] to a maximum of about 2.0 [17]. It has been shown that increases in laser power and decreases in scan speed tend to increase the D/W ratio as a general rule. Additionally, oxygen is known to induce larger ratios for concentrations between an approximate minimum of 0.2% to 0.3% and an approximate maximum of 1.0% to 2.0% oxygen concentration, with lower ratios tending to exist outside of this range [2,3]. This research project aims to fill some of the knowledge gaps which remain. Minimal research exists which specifically targets the influence of oxygen on the D/W ratio of L-PBF additively manufactured stainless steel. There is a notable absence of literature studying the influence of laser power and scanning speed on D/W ratios of L-PBF stainless steel parts as well. This project seeks to fill in the aforementioned gaps in research and thus provide a better understanding of the stainless steel AM L-PBF process.

1.3 Research Purpose and Hypotheses

The purpose of this research is to study the impact of input parameters, namely oxygen concentration, scanning speed, and laser power, on the melt pool morphology

of L-PBF additively manufactured components. To achieve this research goal, it was determined that the specific input parameters of laser power, scan speed, and oxygen concentration, which are known to have influence over the melt pool morphology as discussed in Section 1.2, should be investigated. These parameters were used to develop and define two research hypotheses that were tested systematically as detailed in Section 2 and analyzed in subsequent sections

The first hypothesis was developed based on the environmental factor of oxygen, which is known to affect melt pool morphology.

Research Hypothesis 1: If the environmental oxygen concentration increases, then the depth-to-width (D/W) ratio of a bead will increase.

As shown by previous research projects [1–6,8,9], oxygen generally leads to an increase in the depth-to-width ratio, though a significant drop can occur as the concentration continues to increase. The energy absorption and arc temperature are understood to increase with increasing levels of oxygen. Additionally, the effect of oxygen on the surface tension gradient of the melt pool reverses the Marangoni convection to flow inward, increasing the depth-to-width ratio of the bead.

The second hypothesis was developed from laser power and scan speed, two parameters known to affect the laser energy density.

Research Hypothesis 2: If the scan speed decreases and/or laser power increases, then the D/W ratio of a bead will increase.

This is due to lower speeds resulting in the laser transferring energy to a particular region for a longer period of time, thus increasing the energy absorbed [12,15]. Lower

speeds allow for larger temperature gradients to develop and strengthen the Marangoni convection, increasing the depth-to-width ratio of the bead [7]. As the laser power is increased, more energy from the laser is being transmitted to a particular region, also resulting in an increased amount of energy absorption [14,17].

Our criteria for success will be to achieve consistent variations in the depth-to-width ratio with respect to the input parameters, as this will indicate a strong relationship between the input parameters and the melt pool morphology. The results gathered from the experiments will be used to evaluate the hypotheses and achieve the goal of this project.

The methods used with the goal of achieving the research purpose are discussed in Section 2. The data gathered on input parameters, bead results, and analysis results are highlighted in Section 3. Section 4 is dedicated to a discussion of the results, their significance, and what the next steps should be for future experimentation. Finally, the conclusion gathered from the research project is outlined in Section 5. Any tables, figures, and information referenced but not located in the main body of the paper can be found in Annex A, B, or C.

2. EXPERIMENTAL METHODOLOGY

In order to investigate the issue of the effects of oxygen concentration on melt pool geometry, components were manufactured using a Farsoon FS271M Industrial System L-PBF AM machine under different parametric conditions, in which one machine input parameter was held constant and two machine input parameters were varied according to specific values and combinations. The experiment was designed such that the parameters investigated were the laser power, laser scanning speed, and concentration of oxygen within the build chamber. The component which was manufactured for the first and second

sets of trials consisted of 15 parallel 1.12 in.-long single-bead layers (Figure 1), while the component manufactured for the third trial consisted of 8 parallel 0.56 in.-long single-bead layers. These powderless, single-layer bead-on-plate trials were run in order to evaluate and gain an understanding of L-PBF components at a fundamental level. This foundational knowledge will enable future work with more complex geometries and provide significant input for AM simulations and thermal models.

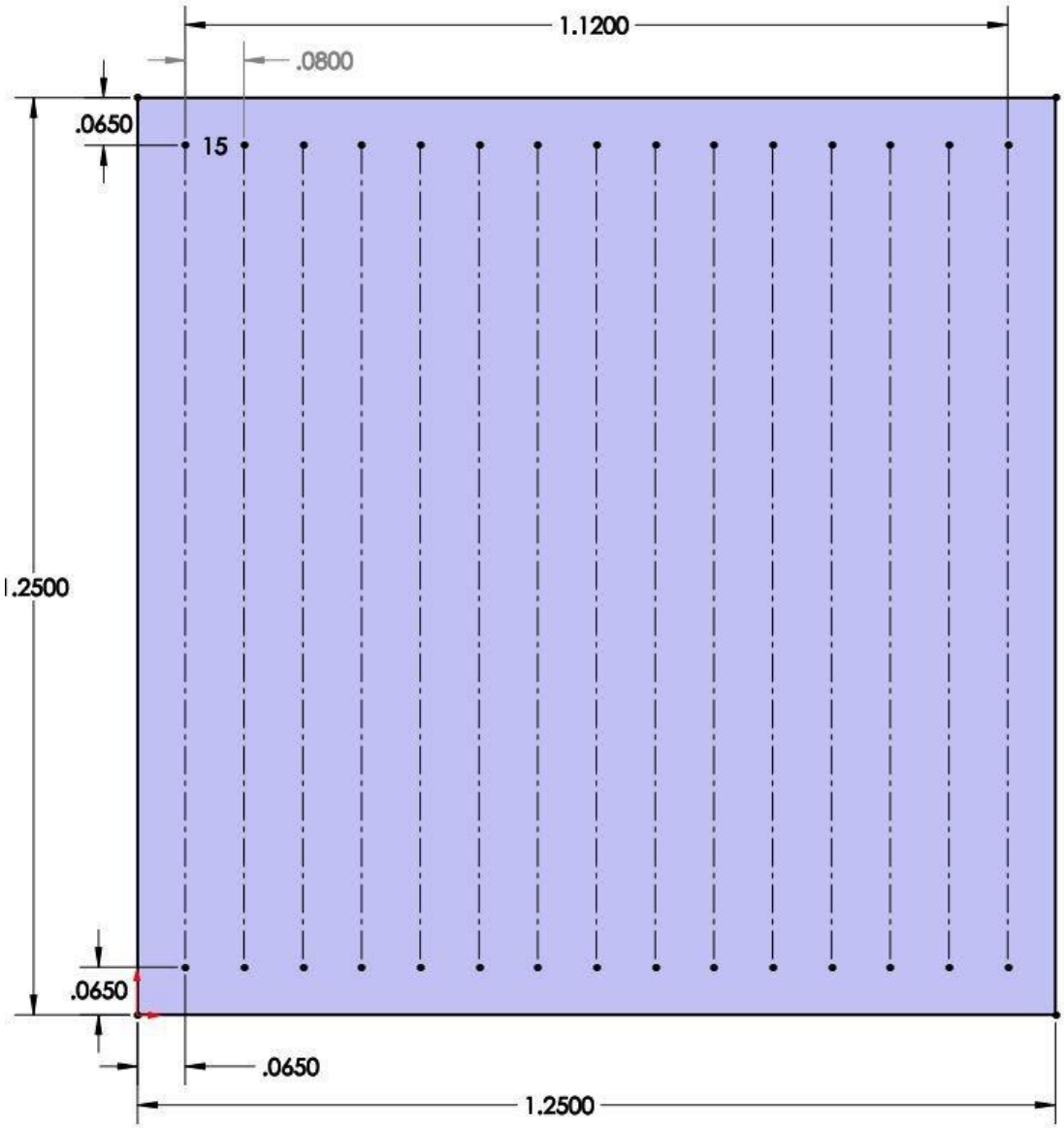

Figure 1. Bead Layout for Sets 1 and 2

The substrates were cut as necessary to a length appropriate to accommodate the L-PBF machine, then cleaned using ethanol and placed in the machine. The bead files were generated using the CAD data for the beads as well as specified input parameters, and the trials were run. A sample code used to manufacture the beads can be found in Appendix C. In order to use the L-PBF machine to manufacture single-layer bead-on-plate trials, several steps were necessary to produce the intended components. A .dbd file was created, and the input variables of start and end locations for the beads, mark speed, pause, etc., were set (Appendix C). This was then uploaded into the MakeStar program in order to run on the machine, while the laser power and oxygen set point were input directly into MakeStar. The oxygen sensor was used to determine the oxygen concentration in the build chamber environment, as well evaluate if the oxygen was well-mixed by analyzing the fluctuations in oxygen readings.

Once the bead-on-plate parts were manufactured, a Mitsubishi wire EDM was used to cut the individual samples from the substrate, with the beads being cut approximately along the bead center and perpendicular to the length. A MetLab MetPress A was used to mount the samples with PSI-202-5 black phenolic mounting powder. For the mounting process, the coolant was turned on and the thermosetting auto setting was used, with the temperature of 195.0 °C, pressure of 290.0 bar, heating time of 8 min., and cooling time of 3 min., with the cooling process set to fast. Once the samples were mounted, they were then ground and polished using a Pace Technologies Nano 1000T Grinder-Polisher and Femto 1100 Polishing Head auto polisher. The samples were ground using 400 grit, 600 grit, and 1200 grit paper, followed by polish with a 3 micron diamond suspension liquid polishing agent. Once the samples were ground and polished until sufficiently smooth to view the beads,

they were etched using the Marble's reagent hydrochloric acid solution. The samples were then analyzed using an Olympus BX53M optical microscope and the Olympus Stream Essentials software were then used to analyze the samples and measure the depths and widths of the beads. A set of example depth and width measurements can be found in Figure 2.

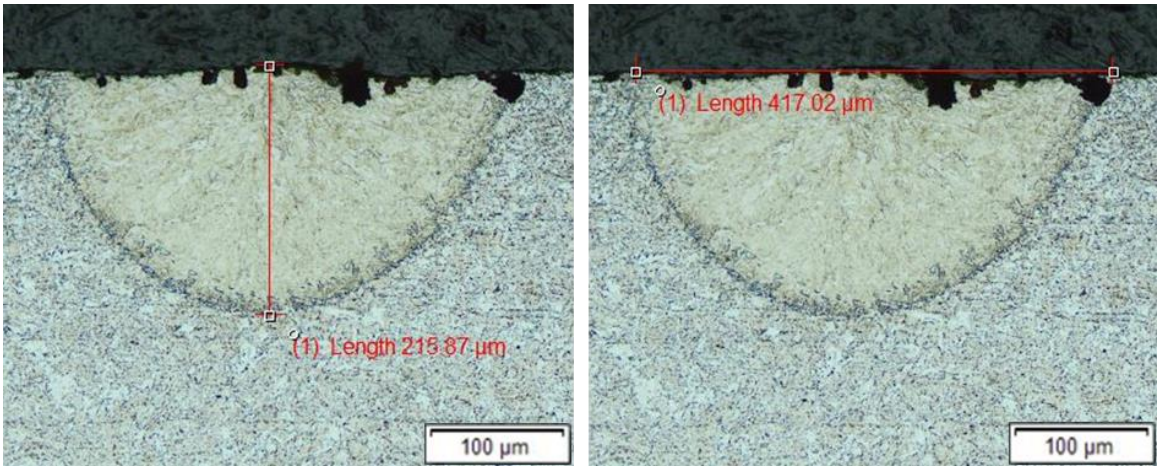

Figure 2. Bead Cross-Section, Trial 2.3, 10x Magnification, Measurement

The first and second sets of trials was kept with a constant ambient oxygen concentration, low and high laser powers of 50 W and 400 W, and low and high scanning speeds of 50 mm/s and 500 mm/s. Thus, a total of four unique machine input parametric conditions were tested, with fifteen beads manufactured at each parametric combination. These conditions were run without metal powder on a low-carbon steel substrate for the first set (Table 1) and a stainless steel substrate for the second set (Table 2) to compare the substrates' responses to the laser in order to determine which substrate material would be more viable for use with further experimentation.

Table 1. First Set – Low Carbon Steel – Settings

Trial	Laser Power (W)	Scanning Speed (mm/s)
1.1	50	50
1.2	50	500
1.3	400	50
1.4	400	500

Table 2. Second Set – Stainless Steel – Settings

Trial	Laser Power (W)	Scanning Speed (mm/s)
2.1	50	50
2.2	50	500
2.3	400	50
2.4	400	500

The samples were then cut, mounted, ground, polished, etched, and analyzed as previously described, and the data was recorded. The figures of the bead cross-sections (Figure 6, Figure 7, Figure 8) can be found in Appendix A, and the tables of input parameter combinations and bead geometry (Table 8, Table 9), can be found in Appendix B. Multiple measurements of the beads were made, and the measurements were statistically analyzed with those from the same bead in order to evaluate the accuracy and precision of the collected data. These averages were then compared with the averages of the other beads to determine which substrate would be better for use in future experiments, as well as to analyze if the power or speed held greater influence over the melt pool morphology.

Upon analysis of the results from the first and second sets of trials, the results regarding substrate sensitivity were inconclusive due to beads from several trials on both substrates being difficult to locate. Of the beads that were locatable, those from the low-carbon steel were better developed than the stainless counterpart. However, as future work will

incorporate stainless steel powder, it was decided that the stainless steel substrate should be used for future experimentation in order to eliminate any anomalies introduced by use of dissimilar materials. Additionally, as the beads manufactured with the high laser power were best developed, it was decided to use a constant high laser power for the third set of trials.

The third set of trials was conducted using a stainless steel substrate and a constant laser power of 400 W, while the oxygen concentration was varied from 0.5% to 3.0% in increments of 0.5%, and the scanning speed was varied from 100 mm/s to 500 mm/s in increments of 200 mm/s (Table 3).

Table 3. Third Set – Stainless Steel – Settings

Trial	Oxygen Concentration (%)	Scanning Speed (mm/s)
3.1	0.5	100
3.2	0.5	300
3.3	0.5	500
3.4	1.0	100
3.5	1.0	300
3.6	1.0	500
3.7	1.5	100
3.8	1.5	300
3.9	1.5	500
3.10	2.0	100
3.11	2.0	300
3.12	2.0	500
3.13	2.5	100
3.14	2.5	300
3.15	2.5	500
3.16	3.0	100
3.17	3.0	300
3.18	3.0	500

The samples were then cut, mounted, ground, polished, etched, and analyzed as previously described, and the data was recorded. Figures of selected bead cross-sections

(Figure 9, Figure 10, Figure 11, Figure 12, Figure 13, Figure 14) can be found in Appendix A, and the tables of input parameter combinations and bead geometry (Table 10, Table 11, Table 12, Table 13, Table 14, Table 15), can be found in Appendix B. Each of the eight beads per trial were measured for depth and width once and then statistically analyzed to determine the average D/W ratio as well as the variation in beads manufactured under the same input parametric conditions.

3. DATA, RESULTS, AND ANALYSIS

3.1 Input Parameter Data

For the first set of trials, the oxygen concentration in the argon/oxygen gas mixture of the build environment was held constant at the ambient level. A low-carbon steel substrate was used for the beads. The laser power was set to 50 W and 400 W, while the scanning speed was set to 50 mm/s and 500 mm/s, yielding a total of four unique trials in the set. The second set of trials was identical to the first, with the exception of a stainless steel substrate being used as opposed to a low-carbon steel material. The third set of trials used a stainless steel substrate and a constant laser power of 400 W. For this set, the oxygen concentration was set to values of 0.5%, 1.0%, 1.5%, 2.0%, 2.5%, and 3.0% of the build environment, and the scanning speed was set to 100 mm/s, 300 mm/s, and 500 mm/s. This resulted in 18 unique trials in the third set. The oxygen levels within the build chamber at the time of manufacture were measured via a sensor and can be found in Table 4. The percent error between the theoretical target oxygen concentrations and experimentally determined oxygen concentrations for trial set 3 was calculated using Equation 1.

$$\%Error = \frac{|theoretical - experimental|}{theoretical} \cdot 100\% \quad (1)$$

Table 4. Theoretical and Experimental Oxygen Concentrations, First Set

Trial	Scan Speed (mm/s)	Oxygen Concentration, Theoretical (%)	Oxygen Concentration, Sensor (%)	%Error
3.1	100	0.5	0.49	2.00%
3.2	300	0.5	0.50	0.00%
3.3	500	0.5	0.50	0.00%
3.4	100	1.0	0.99	1.00%
3.5	300	1.0	0.99	1.00%
3.6	500	1.0	0.99	1.00%
3.7	100	1.5	1.51	0.67%
3.8	300	1.5	1.50	0.00%
3.9	500	1.5	1.51	0.67%
3.10	100	2.0	2.00	0.00%
3.11	300	2.0	1.99	0.50%
3.12	500	2.0	1.99	0.50%
3.13	100	2.5	2.50	0.00%
3.14	300	2.5	2.51	0.40%
3.15	500	2.5	2.50	0.00%
3.16	100	3.0	2.99	0.33%
3.17	300	3.0	2.97	1.00%
3.18	500	3.0	3.00	0.00%

3.2 Experimental Results and Analysis

The depth-to-width ratios were evaluated using Equation 2 using the measured depths and widths of the bead cross-section.

$$D/W = \frac{depth}{width} \quad (2)$$

Averages were determined via Equation 3.

$$\overline{x} = \frac{\sum_{i=1}^{N} x_i}{N} \quad (3)$$

The population standard deviation was used to determine the uncertainty within a single measurement type and was calculated using Equation 4.

$$\sigma = \sqrt{\left|\frac{\Sigma_{i=1}^{N}(x_i - \overline{x})^2}{N}\right|} \quad (4)$$

4. DISCUSSION

4.1 First and Second Sets of Trials

Regarding substrate material, the beads manufactured on the low-carbon steel substrate were better developed. However, future work involving powder will use stainless steel as the metal powder. Thus, it was decided that stainless steel would be the substrate for subsequent trials in order to eliminate any anomalies introduced by dissimilar materials. For the low power trials and high speed trials with the low-carbon steel substrate, the bead locations were inconclusive, so the ratio was not determined (Table 8). For the high power and high speed, the average depth-to-width ratio was 1.01 (Table 8). For the first set of trials, the median of the D/W ratios used to determine the average was found to be 1.01, with a range of 0.20, and standard deviation of 0.07 (Table 5). Thus, while the individual ratios had a notable difference between the maximum and minimum D/W ratios, the average yielded an accurate depiction of the ratios, and there was minimal spread in the data.

For the stainless steel substrate, the low power and low speed combination, as well as the low power and high speed combination, yielded beads which were not locatable, and thus depth-to-width data was not gathered (Table 9). The high power and low speed resulted in an average depth-to-width ratio of 0.54, while the high power and high speed resulted in an average D/W ratio of 0.44 (Table 6). For trial 2.3, the median D/W ratio,

range, and standard deviation were determined to be 0.53, 0.03, and 0.01, respectively (Table 6). The median D/W ratio, range, and standard deviation for trial 2.4 were calculated and found to be 0.44, 0.11, and 0.04, respectively (Table 6). As with the first trial set, the similarity between average and median D/W values indicated that the average closely represented the central tendency of the individually measured D/W values. The range for trial 2.3 indicated very little spread between the maximum and minimum D/W ratios, while trial 2.4 exhibited a larger difference. However, the low standard deviation showed that the overall spread in data was small.

Based on the data, it was determined that the high laser power yielded the best results, given that the ideal D/W ratio was between values of 0.5 and 2.0 as previously discussed in Section 1.2. This information was used to select a constant laser power of 400 W for the third set of trials, with the scanning speed and oxygen concentration being varied according to Table 3.

Table 5. Statistical Analysis, First Set

Trial	Average D/W	Median D/W	Range D/W	Standard Deviation
1.1	N/A	N/A	N/A	N/A
1.2	N/A	N/A	N/A	N/A
1.3	N/A	N/A	N/A	N/A
1.4	1.01	1.01	0.20	0.07

Table 6. Statistical Analysis, Second Set

Trial	Average D/W	Median D/W	Range D/W	Standard Deviation
2.1	N/A	N/A	N/A	N/A
2.2	N/A	N/A	N/A	N/A
2.3	0.53	0.53	0.03	0.01
2.4	0.44	0.44	0.11	0.04

4.2 Third Set of Trials

In order to determine the accuracy of the environmental oxygen levels measured at the time of manufacture, these recorded values were compared with the theoretical oxygen levels by determining the percent error (Table 4). The small percent error, which ranged from 0.00% to 2.00%, indicated that the actual oxygen levels present at the time of bead manufacture was accurate with respect to the intended theoretical oxygen levels. For the third set of bead-on-plate trials run, the average D/W ratio of the eight beads from a trial were calculated and the and the values can be found in Table 10, Table 11, Table 12, Table 13, Table 14, and Table 15. The average D/W ratios for this trial set varied from 0.38 to 0.84. The median values for the third trial set tended to closely follow the average D/W ratios calculated (Table 7) with the average and median ratios differing by amounts between 0.00 and 0.07. This indicated an absence of outlier D/W ratios and that the average adequately represents the data of each trial. However, the ranges were notably larger, with values from 0.12 to 0.68, thus showing that while outlier data points were absent, the data exhibited spread. The standard deviations of the average D/W ratios for the third set of trials ranged from 0.03 to 0.23 (Table 7), with an average standard deviation of 0.10.

Table 7. Statistical Analysis, Third Set

Trial	Average D/W	Median D/W	Range D/W	Standard Deviation
3.1	0.74	0.73	0.25	0.08
3.2	0.84	0.86	0.25	0.06
3.3	0.49	0.46	0.29	0.05
3.4	0.77	0.76	0.25	0.03
3.5	0.84	0.82	0.29	0.07
3.6	0.38	0.36	0.14	0.08
3.7	0.74	0.76	0.68	0.10
3.8	0.84	0.84	0.25	0.11
3.9	0.48	0.51	0.36	0.10
3.10	0.65	0.66	0.38	0.09
3.11	0.78	0.79	0.36	0.08
3.12	0.40	0.42	0.27	0.08
3.13	0.71	0.78	0.35	0.08
3.14	0.74	0.76	0.42	0.08
3.15	0.41	0.40	0.27	0.05
3.16	0.69	0.71	0.43	0.18
3.17	0.63	0.64	0.46	0.23
3.18	0.41	0.42	0.12	0.22

From the third set of trials, it was discovered that the oxygen concentration had a notable correlation to the D/W ratio of the bead (Figure 3). Using Microsoft Excel, the lines of best fit were determined to be Equation 5 with an $R^2 = 0.4392$ for 100 mm/s, Equation 6 with an $R^2 = 0.9908$ for 300 mm/s, and Equation 7 with an $R^2 = 0.2178$ for 500 mm/s. For the three constant scan speeds, the peak average D/W ratio occurred within oxygen concentrations of 0.5% to 1.5%, with a drop at the 2.0% oxygen level.

$$y = 0.0111x2 - 0.0686x + 0.7955 \quad (5)$$

$$y = -0.0513x2 + 0.0995x + 0.7992 \quad (6)$$

$$y = 0.0141x2 - 0.0688x + 0.4934 \quad (7)$$

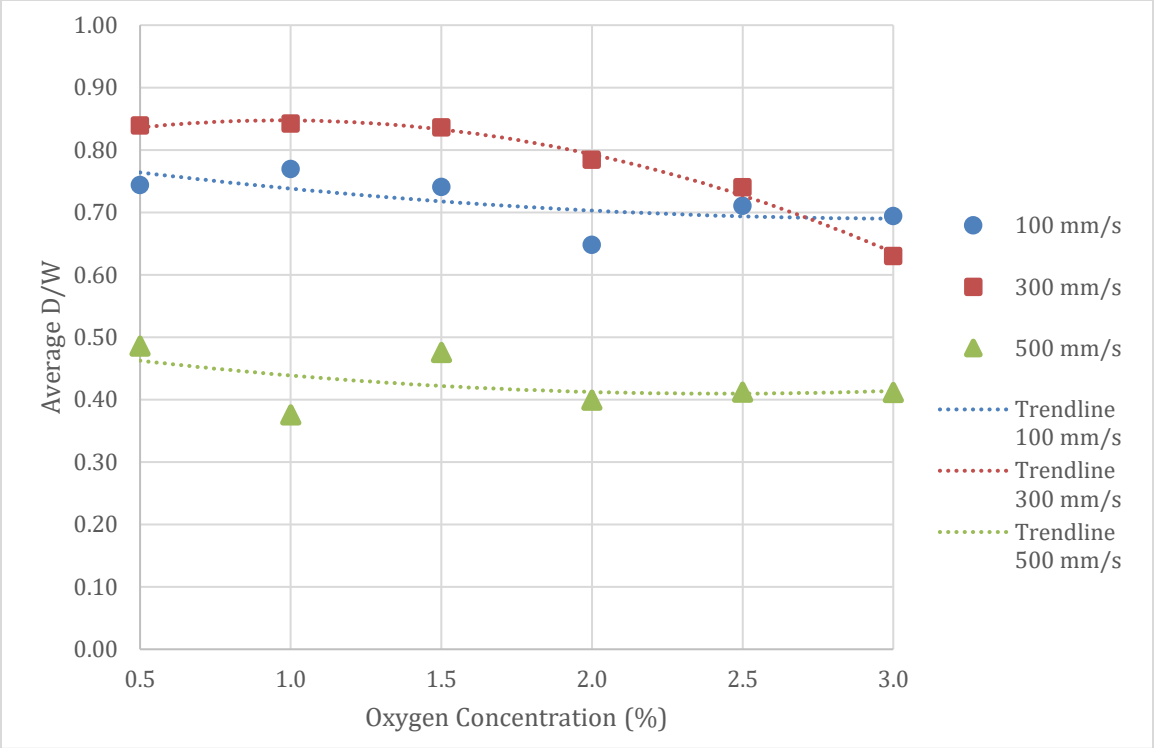

Figure 3. Average D/W vs. Oxygen

A strong polynomial relationship was seen between the weld bead morphology and the scan speed, as seen in Figure 4. Equations 8-13 mathematically represent the trends for oxygen concentrations 0.5% through 3.0%, respectively. The R squared values were found to be equal to 1 for all oxygen concentrations. For the scan speeds analyzed, it appeared that the largest average D/W ratios occurred within the range of 100 mm/s to 300 mm/s. An exception may be the beads manufactured at 3.0% oxygen, as these ratios may peak at a scan speed less than what was covered in this research project.

$$y = -6E-06x2 + 0.0027x + 0.5279 \quad (8)$$

$$y = -7E-06x2 + 0.0031x + 0.5306 \quad (9)$$

$$y = -6E-06x2 + 0.0028x + 0.5222 \quad (10)$$

$$y = -7E-06x2 + 0.0033x + 0.3839 \quad (11)$$

$$y = -4E-06x2 + 0.0019x + 0.5614 \quad (12)$$

$$y = -2E-06x2 + 0.0005x + 0.6683 \quad (13)$$

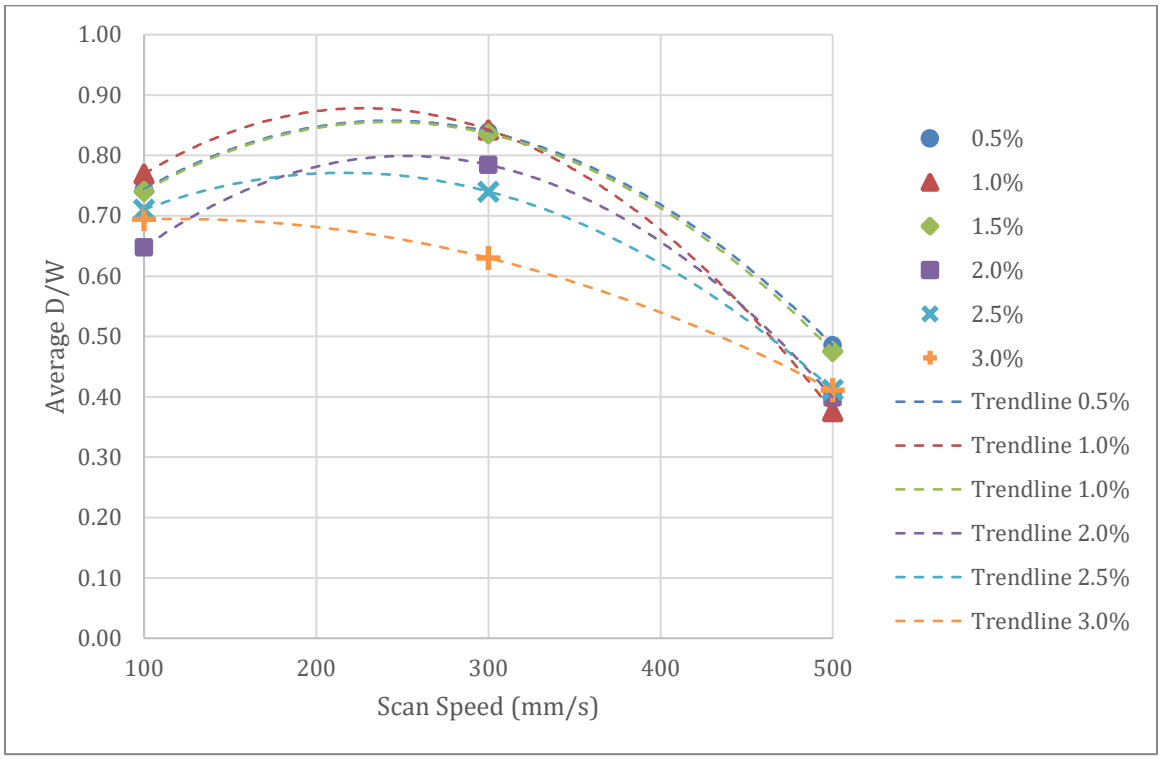

Figure 4. Average D/W vs. Scan Speed

The largest difference between trend lines was determined to be between those for the 2.0% and 3.0% constant oxygen concentration data sets (Figure 4, Figure 5). With the exception of the trials run at 2.0% oxygen, the trends suggested that as the presence of oxygen in the build environment increased, the D/W ratio peaked at lower scanning speeds.

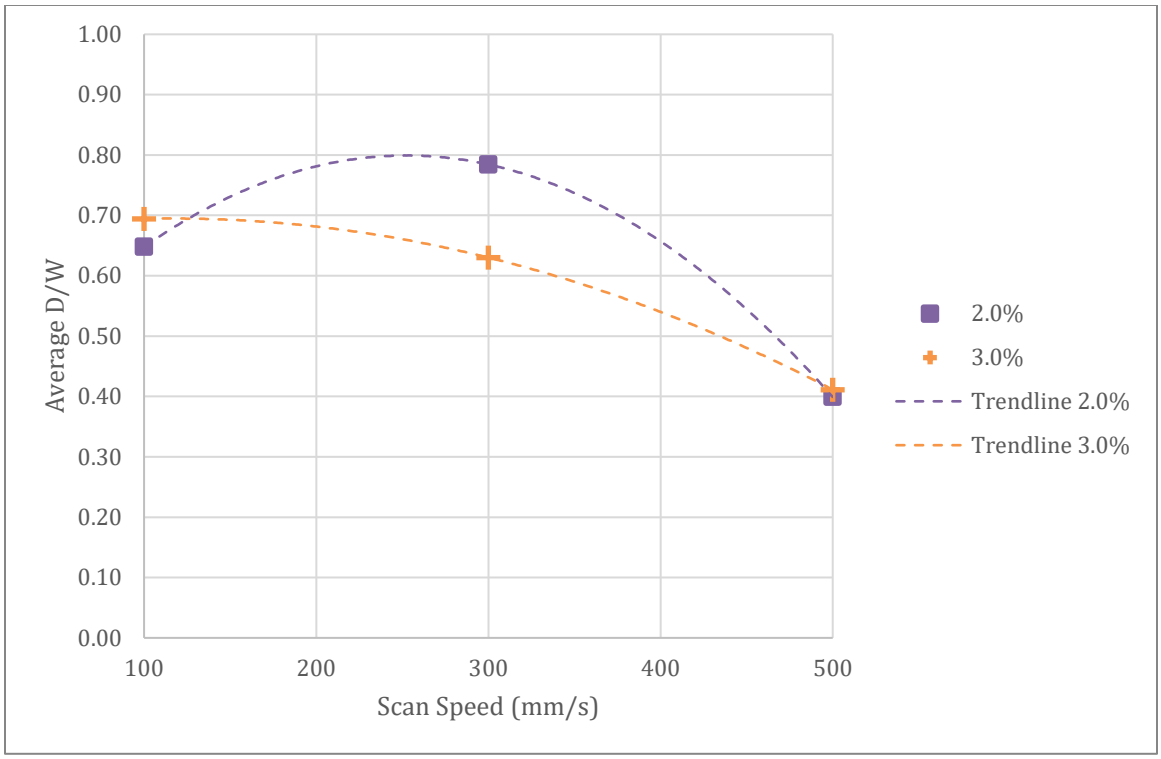

Figure 5. Average D/W vs. Scan Speed, Comparison

The standard deviations for the average D/W ratios run at 100 mm/s, 300 mm/s, and 500 mm/s are shown in Figure 15, Figure 16, and Figure 17 in Appendix B. There was no clear trend between magnitude of standard deviations and oxygen concentrations which held for all scan speeds (Figure 15, Figure 16, Figure 17). However, it was noted that while the distribution of standard deviation magnitude appeared random for constant speeds of 100 mm/s and 500 mm/s, a distinct trend of increasing standard deviations for increasing oxygen concentrations was discovered for the 300 mm/s scan speed data. Additionally, the trials manufactured at 100 mm/s and 500 mm/s both exhibited large standard deviations for the oxygen concentration of 1.5%, while those manufactured at the scan speed of 300 mm/s did not exhibit this spike in magnitude.

The standard deviations were also shown with the average D/W ratios run at 0.5% though 3.0% and can be found in Figure 18, Figure 19, Figure 20, Figure 21, Figure 22, and Figure 23 in Appendix B. Based on the error bar depiction of the standard deviations for the average ratios vs. the scan speeds, it was noted that the standard deviations exhibited some tendency to increase as the oxygen concentration increased (Figure 18, Figure 19, Figure 20, Figure 21, Figure 22, Figure 23). This tendency was also noted in the graphs for average ratios vs. oxygen concentrations at constant speeds of 100 mm/s and 300 mm/s (Figure 15, Figure 16), although the graph of ratios vs oxygen at a constant 500 mm/s speed did not exhibit this trend (Figure 17). This may have been the result of issues in mixing the oxygen with argon in the build environment. During the experimental procedure, it was noted from the oxygen sensor that the oxygen levels tended to fluctuate more noticeably for higher oxygen levels, and that some degree of lag was present in the sensor display, potentially impacting the recorded oxygen measurements. It was also found to be of note that the 500 mm/s scan speed generally had the smallest standard deviation for any given oxygen concentration.

The overall purpose of this research was to study the impact of input parameters, namely oxygen concentration, scanning speed, and laser power, on the melt pool morphology of L-PBF additively manufactured components. This was achieved by developing and testing two research hypotheses, which were: 1) if the environmental oxygen concentration increases, then the depth-to-width (D/W) ratio of a bead will increase, and 2) if the scan speed decreases and/or laser power increases, then the D/W ratio of a bead will increase. The experiment would be deemed successful if the hypotheses were shown to be true and if the statistical analysis supported the significance of the results.

In the third set of trials, an increase in the D/W ratio due to an increasing concentration of oxygen was suggested by the data, up to approximately 1.5% oxygen. After this point, a trend of decreasing ratios was found for increasing oxygen levels. The depth-to-width ratio was found to increase with decreasing scanning speeds in the third set of trials as well. However, for speeds less than approximately 300 mm/s, a correlation was discovered in which increased scan speeds yielded increased D/W ratios. The depth-to-width ratio was found to increase with increasing laser power from trial set 2, as the high laser power yielded ratios, while the low powers produced unlocatable beads. Thus, the data collected was in accordance with hypotheses put forth in Section 1.3. The average and median depth-to-width ratios had minimal difference, indicating that the average was a good representation of each set. The ranges varied, showing that some ratios had little spread between the maximum and minimum ratios collected, while others exhibited greater variation between these values. The standard deviation demonstrated that most samples had data closely clustered about the mean, but an increase in spread was exhibited by the trials run with 3.0% oxygen concentration. Thus, it was concluded that the statistical analysis supports the significance of the data gathered, which in turn was in agreement with the proposed hypotheses. Based on these factors, the purpose of this research project was achieved, and the project deemed successful.

There are several ways in which the experiment conducted could be improved upon in future work. While the substrate material was cleaned with ethanol before use, a more intensive clean would have removed additional contaminants. The L-PBF machine used had stainless steel powder in the bed, which was moved within the build environment by the fan that mixed the oxygen and argon in the chamber. Thus, errors in the results may be

present due to small amounts of powder potentially being blown across the substrate as the laser passed over the material. Additionally, based on the readings of sensors located at the inlet and outlet for argon, as well as the build chamber top, the oxygen did not fully mix with the argon, resulting in alternating spikes and dips in oxygen levels at different locations and at different times. While the fan aided in the mixing of the two gases, additional measures, such as an additional fan, controlled oxygen inlet and outlet, or allowing the gases to mix for a longer period of time before running a trial, should be taken. Given that insufficient data regarding the influence of laser power on melt pool morphology was collected, an additional set of trials should be conducted to investigate this particular input parameter.

The goal of this research project was to determine how oxygen concentration determines the resultant geometry and mechanical properties of L-PBF additively manufactured components. While progress has been made in studying the effects of oxygen concentration, laser power, and scanning speed on the morphology of components manufactured via L-PBF, additional work should be performed to generate a clearer picture of the relation between the input parameters and final product. Thus, future work will include using the data and results from this project to determine how to best fine-tune input parameters in order to achieve the most desirable product. Additionally, more complex components will be manufactured, as opposed to single-stripe beads, in order to develop a more robust understanding of how bead layers interact with each other while also being impacted by changes in the three input parameters studied in this project. Future study should also include an investigation into how the input parameters discussed in this project

influence the surface roughness of L-PBF AM components so that the mechanical properties of such products can be more thoroughly understood.

5. CONCLUSION

The purpose of this experiment was to determine how melt pool geometry was influenced by oxygen concentration, laser power, and scanning speed. Testing was conducted to first determine what combinations of laser power and scanning speed would produce the best D/W ratios at constant oxygen concentrations, as well as to determine whether low-carbon steel or stainless steel would be better for use as the substrate material The oxygen concentration was maintained constant at an ambient level, while the laser power was varied at 50 W and 400 W, the scanning speed was varied at 50 mm/s and 500 mm/s, and the substrate materials used were low-carbon steel and stainless steel. The beads from the 1.1, 1.2, 1.3, 2.1, and 2.2 trials were not locatable. The beads from trials 1.4, 2.3, and 2.4 were determined to have average D/W ratios of 1.01, 0.53, and 0.44, respectively. From these results, it was discovered that the low-carbon steel substrate produced a more desirable D/W ratio for the bead. However, it was decided to use the stainless steel substrate for further experimentation in order to avoid complications from dissimilar materials as future work will incorporate stainless steel powder. Additionally, based on the data, it was discovered that the 400 W laser power trials generally yielded more desirable beads, while the 50 W laser power trials tended to yield unlocatable beads. Given the strength of the power-to-D/W correlation over that of the speed-to-D/W correlation, it was determined that the next set of trials would use a constant high laser power of 400 W while varying oxygen concentration from 0.5% to 3.0%, in increments of 0.5%, and scanning speed from 100 mm/s to 500 mm/s, in increments of 200 mm/s. Once this was determined, the third

set of trials was conducted and analyzed. Across almost all oxygen levels, the D/W ratios exhibited a trend of marginal increase followed by a marked decreased for any given scan speed. The trials conducted with 2.0% exhibit this trend, as the ratios were 0.65, 0.78, and 0.40 for increasing scan speeds. The exception to this trend was the trials manufactured at 3.0% oxygen, which had ratios of 0.69, 0.63, and 0.41 for the scan speeds of 100 mm/s, 300 mm/s, and 500 mm/s, respectively. While the standard deviations fluctuated randomly in general, it was of note that those run at 300 mm/s exhibited consistent deviations for lower oxygen concentrations, which then increased and remained consistent for oxygen levels at and above 2.0%. For the trials manufactured at scan speeds of 100 mm/s and 500 mm/s, a sudden increase in magnitude of the standard deviation occurred at a concentration of 1.5% oxygen. These interesting trends may have been the result of issues in mixing the oxygen with argon in the build environment for the higher oxygen concentrations, as well as lag inherent in the oxygen sensor.

The first trial set could not confirm nor contradict the hypotheses as only one trial from the set had a clear bead cross-section and thus could not be compared against another trial within the same set. The second trial set confirmed the hypothesis that increased laser power resulted in larger ratios. Additionally, the D/W ratio data gathered from both the second and third sets of trials confirmed both of the hypotheses presented previously, in which incrementally lower laser powers, as well as incrementally higher scanning speeds and oxygen concentrations, would yield larger depth-to-width ratios. The data was supported by acceptably low standard deviations, indicating that the average ratios were indicative of the overall collected data.

REFERENCES

[1] Heiple, C. R., and Burgardt, P., 1985, “Effects of So//2 Shielding Gas Additions on Gta Weld Shape.,” Weld. J. (Miami, Fla), **64**(6), pp. 2–5.

[2] Lu, S. P., Fujii, H., Nogi, K., and Sato, T., 2007, “Effect of Oxygen Content in He-O2 Shielding Gas on Weld Shape in Ultra Deep Penetration TIG,” Sci. Technol. Weld. Join., **12**(8), pp. 689–695.

[3] Lu, S., Fujii, H., and Nogi, K., 2006, “Marangoni Convection and Gas Tungsten Arc Weld Shape Variations on Pure Iron Plates,” ISIJ Int., **46**(2), pp. 276–280.

[4] Heiple, C. R., and Roper, J. R., 1982, “Mechanism for Minor Element Effect on Gta Fusion Zone Geometry.,” Weld. J. (Miami, Fla), **61**(4).

[5] Naito, Y., Mizutani, M., and Katayama, S., 2006, “Effect of Oxygen in Ambient Atmosphere on Penetration Characteristics in Single Yttrium–Aluminum–Garnet Laser and Hybrid Welding,” J. Laser Appl., **18**(1), pp. 21–27.

[6] Unni, A. K., and Vasudevan, M., 2019, “Numerical Modelling of Fluid Flow and Weld Penetration in Activated TIG Welding,” Mater. Today Proc., **27**(September), pp. 2768–2773.

[7] Dong, W., Lu, S., Li, D., and Li, Y., 2011, “GTAW Liquid Pool Convections and the Weld Shape Variations under Helium Gas Shielding,” Int. J. Heat Mass Transf., **54**(7–8), pp. 1420–1431.

[8] Tathgir, S., Bhattacharya, A., and Bera, T. K., 2015, “Influence of Current and Shielding Gas in TiO2 Flux Activated Tig Welding on Different Graded Steels,” Mater. Manuf. Process., **30**(9), pp. 1115–1123.

[9] Zacharia, T., David, S. A., Vitek, J. M., and Debroy, T., 1989, “Weld Pool

Development during GTA and Laser Beam Welding of Type 304 Stainless Steel Part II. Experimental Correlation," Weld. J. (Miami, Fla), **68**(12), pp. 510–520.

[10] Matilainen, V., Piili, H., Salminen, A., Syvänen, T., and Nyrhilä, O., 2014, "Characterization of Process Efficiency Improvement in Laser Additive Manufacturing," Phys. Procedia, **56**(C), pp. 317–326.

[11] Pixner, F., Warchomicka, F., Peter, P., Steuwer, A., Colliander, M. H., Pederson, R., and Enzinger, N., "Wire-Based Additive Manufacturing of Ti-6Al-4V Using Electron Beam Technique," pp. 1–23.

[12] Lee, Y., Zhuang, J., Hsieh, W., and Yang, A., 2017, "FEM Simulations to Study the Effects of Laser Power and Scan Speed on Molten Pool Size in Additive Manufacturing," Int. J. Mech. Mechatronics Eng., **11**(7), pp. 1298–1302.

[13] Dilip, J. J. S., Zhang, S., Teng, C., Zeng, K., Robinson, C., Pal, D., and Stucker, B., 2017, "Influence of Processing Parameters on the Evolution of Melt Pool, Porosity, and Microstructures in Ti-6Al-4V Alloy Parts Fabricated by Selective Laser Melting," Prog. Addit. Manuf., **2**(3), pp. 157–167.

[14] Nam, S., Cho, H., Kim, C., and Kim, Y. M., 2018, "Effect of Process Parameters on Deposition Properties of Functionally Graded STS 316/Fe Manufactured by Laser Direct Metal Deposition," Metals (Basel)., **8**(8).

[15] Gupta, S. K., Mehrotra, S., Raja, A. R., Vashista, M., and Yusufzai, M. Z. K., 2019, "Effect of Welding Speed on Weld Bead Geometry and Percentage Dilution in Gas Metal Arc Welding of SS409L," Mater. Today Proc., **18**, pp. 5032–5039.

[16] Scime, L., and Beuth, J., 2019, "Melt Pool Geometry and Morphology Variability for the Inconel 718 Alloy in a Laser Powder Bed Fusion Additive Manufacturing

Process," Addit. Manuf., **29**(July), p. 100830.

[17] Narra, S. P., 2017, "Melt Pool Geometry and Microstructure Control Across Alloys in Metal Based Additive Manufacturing Processes," Dissertations.

APPENDIX A

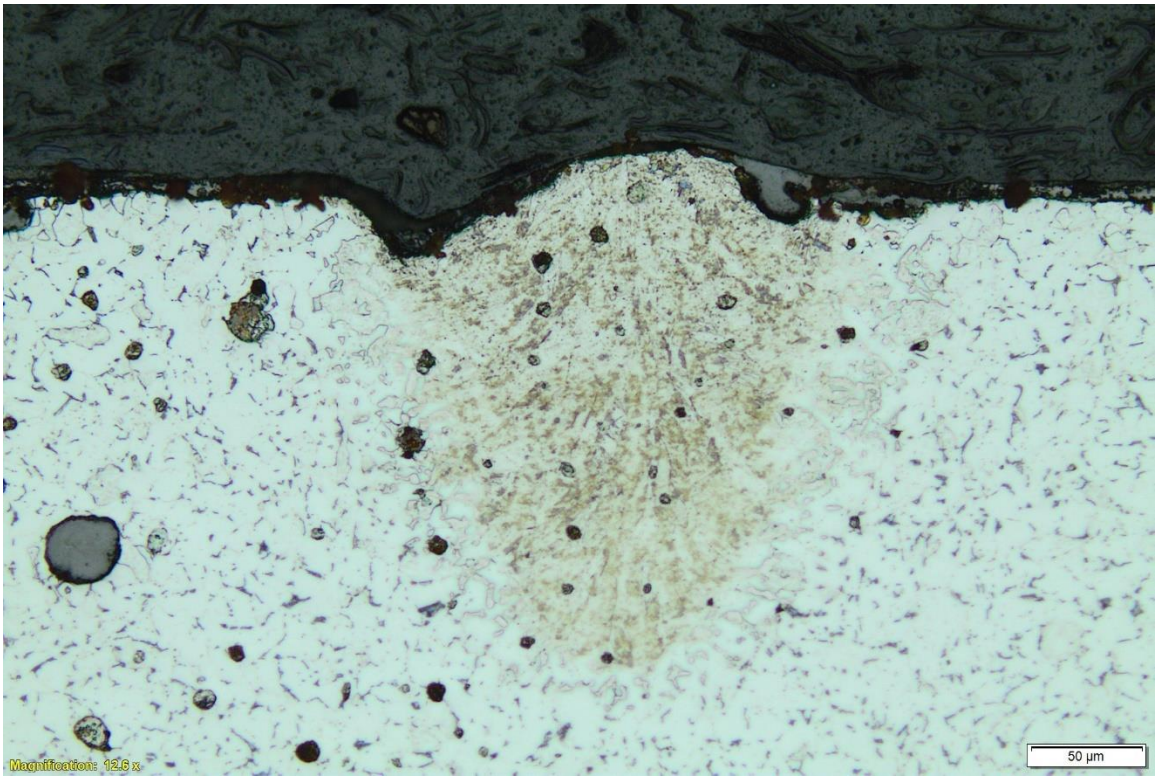

Figure 6. Bead Cross-Section, Trial 1.4, 20x Magnification

Figure 7. Bead Cross-Section, Trial 2.3, 20x Magnification

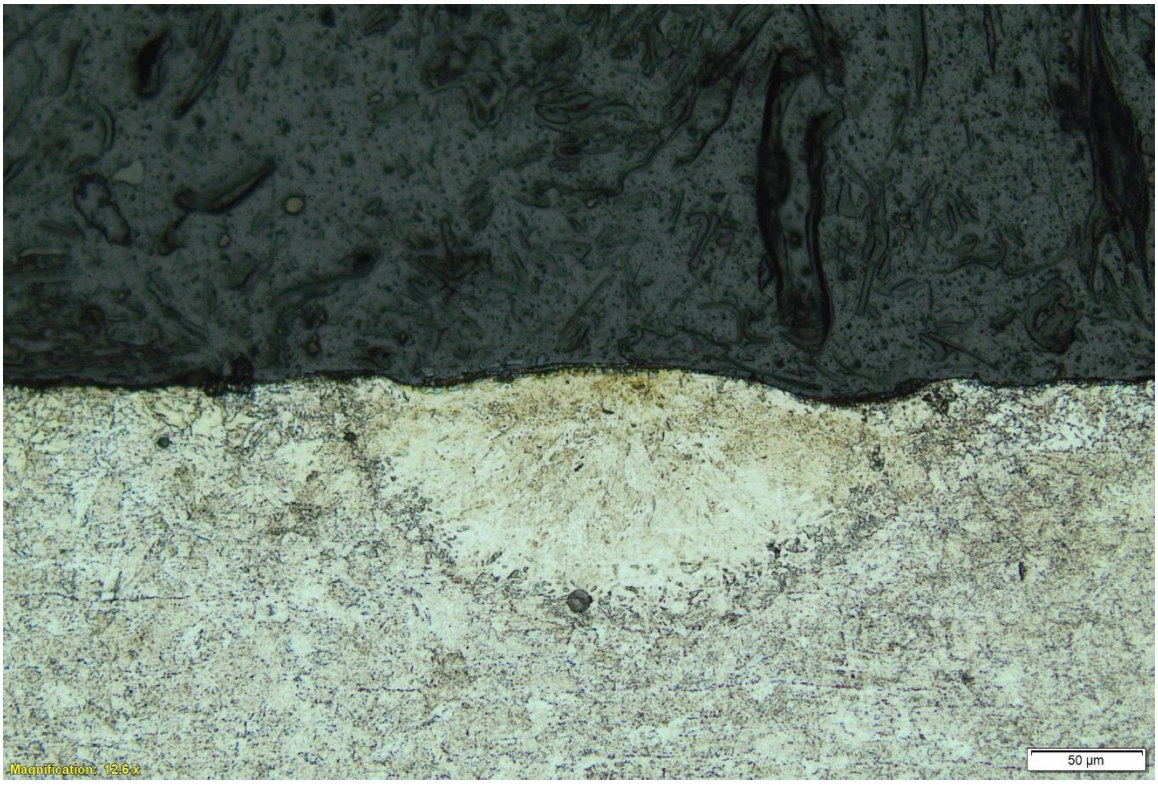

Figure 8. Bead Cross-Section, Trial 2.4, 20x Magnification

Figure 9. Bead Cross-Section, Trial 3.7, 10x Magnification, Bead 4

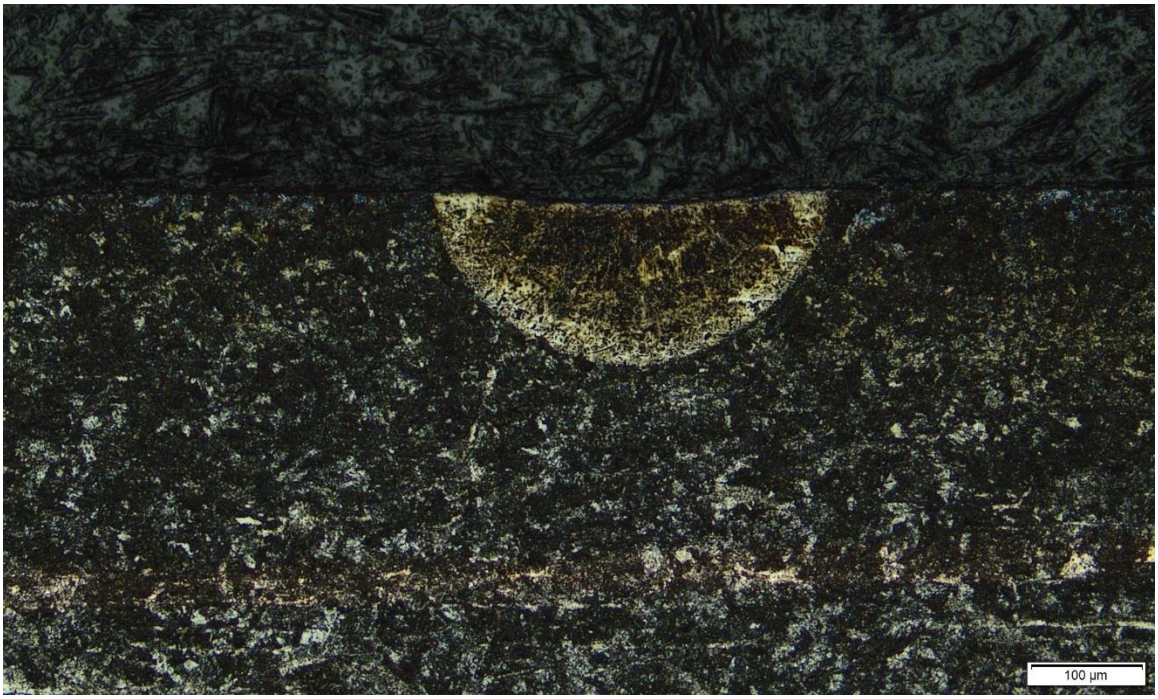

Figure 10. Bead Cross-Section, Trial 3.7, 10x Magnification, Bead 6

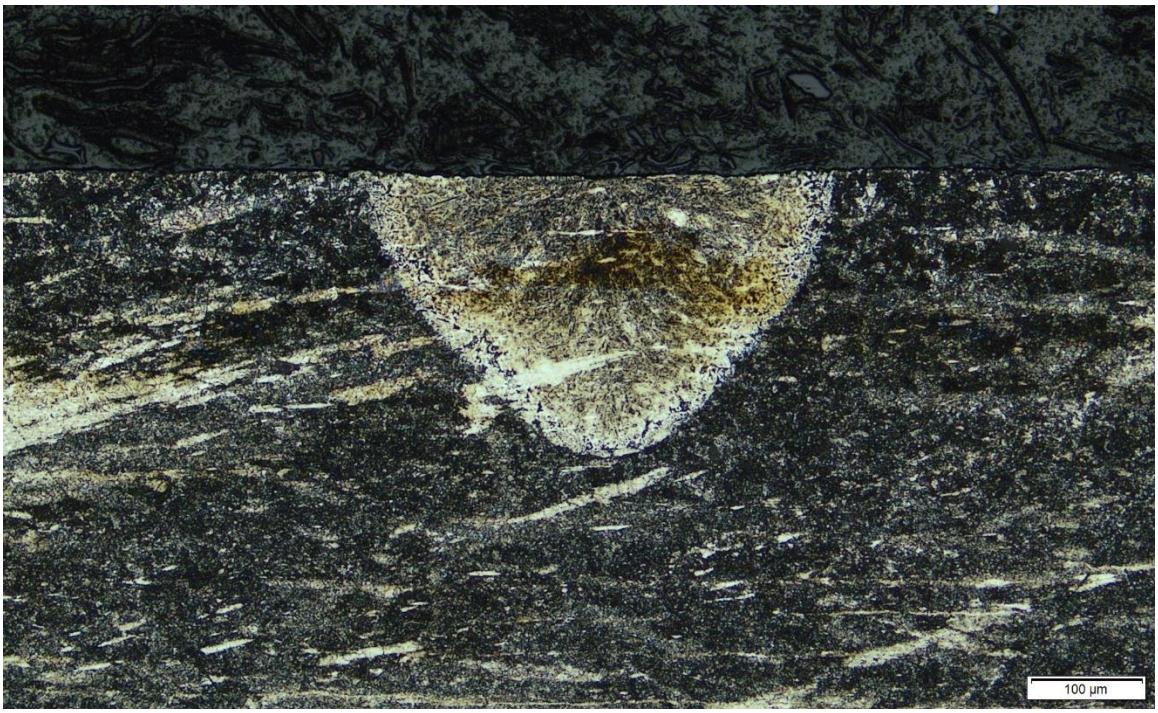

Figure 11. Bead Cross-Section, Trial 3.11, 10x Magnification, Bead 1

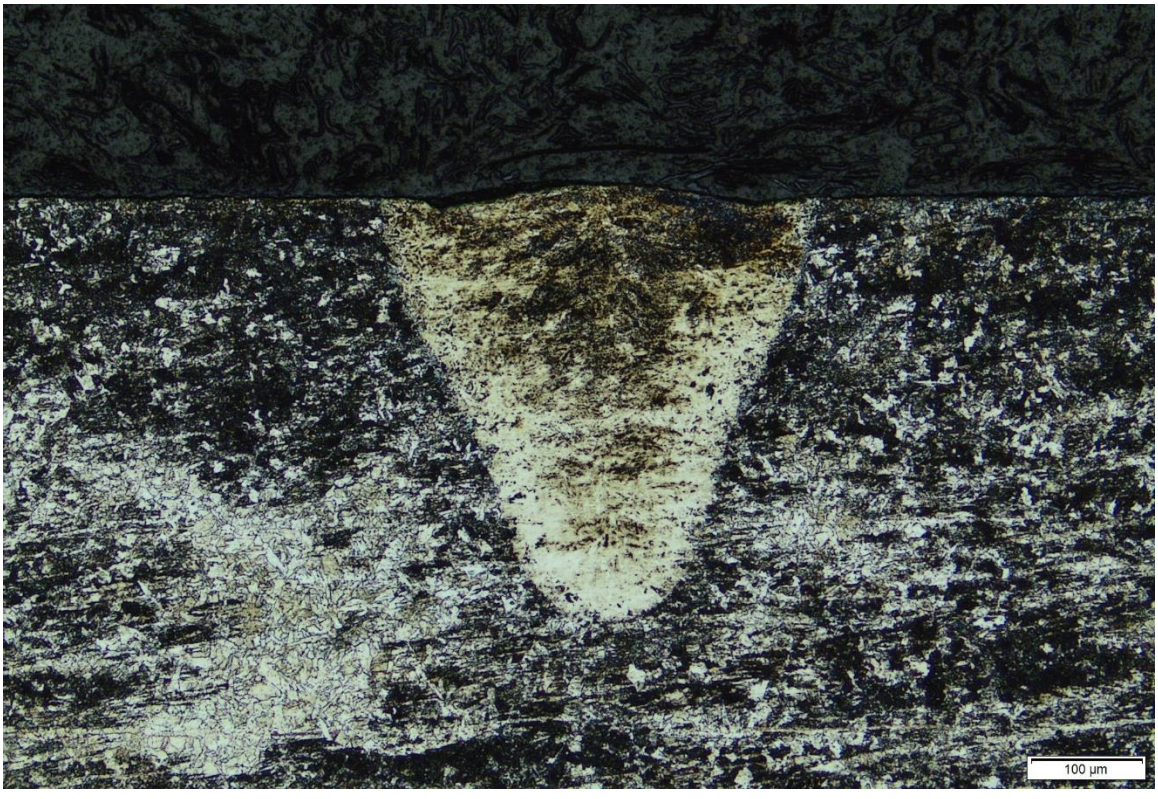

Figure 12. Bead Cross-Section, Trial 3.11, 10x Magnification, Bead 7

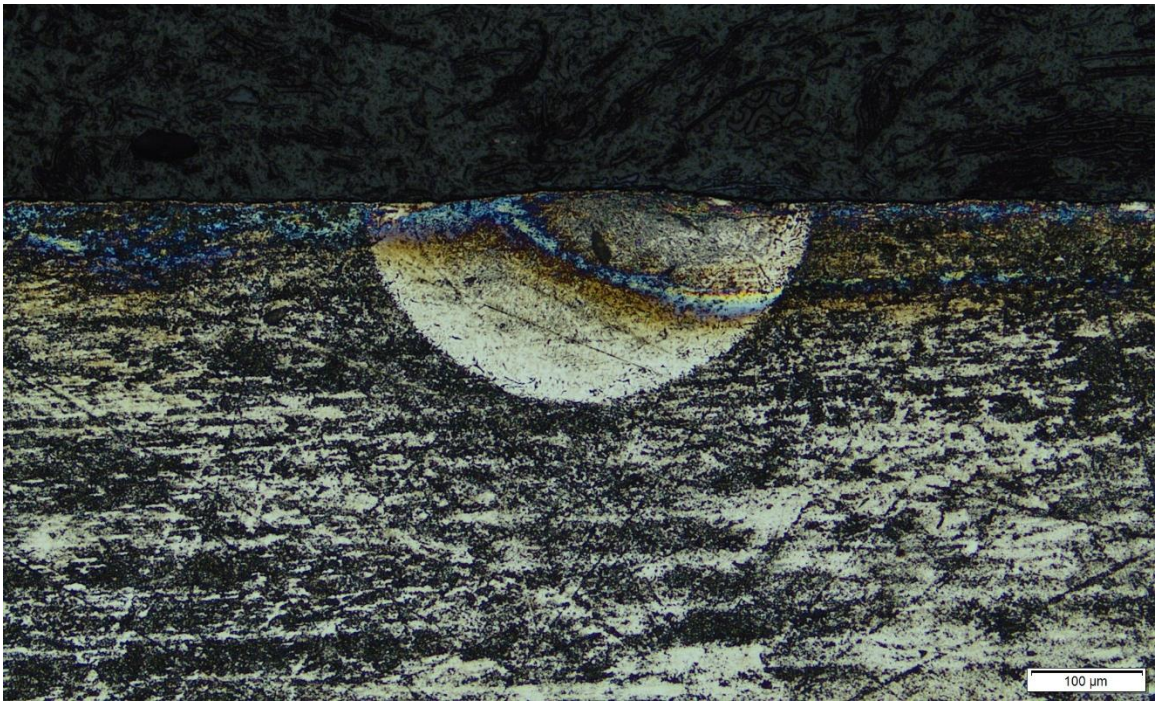

Figure 13. Bead Cross-Section, Trial 3.16, 10x Magnification, Bead 2

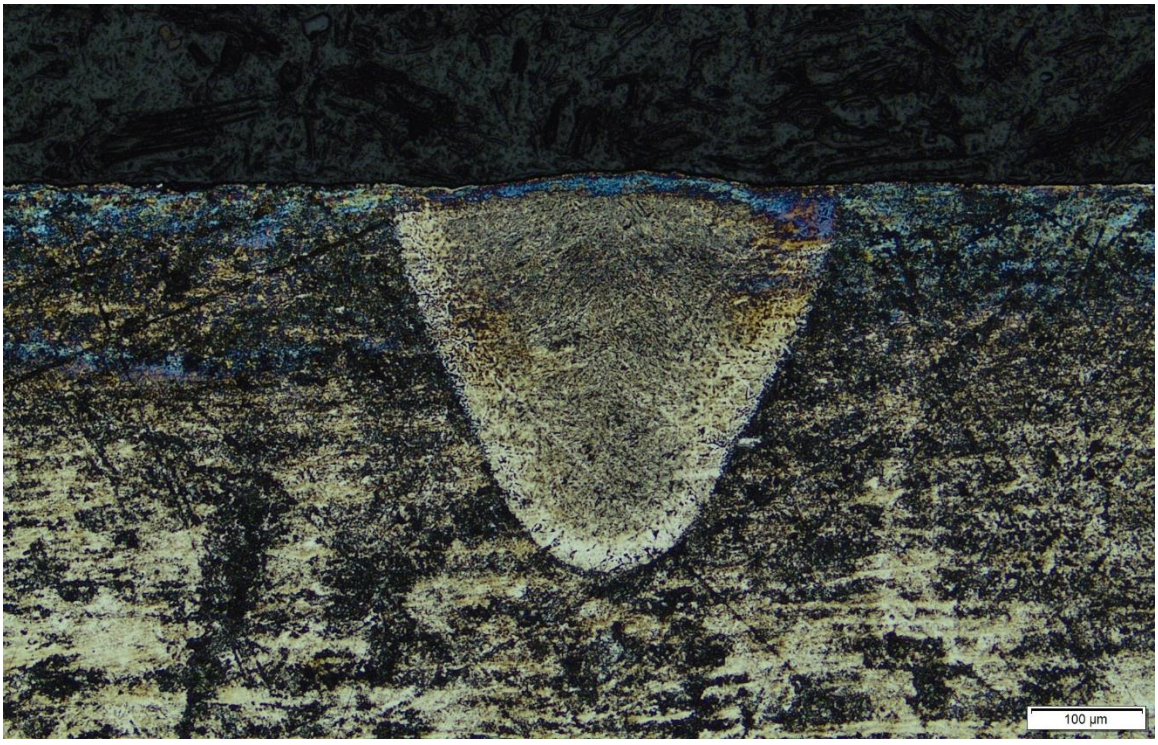

Figure 14. Bead Cross-Section, Trial 3.16, 10x Magnification, Bead 4

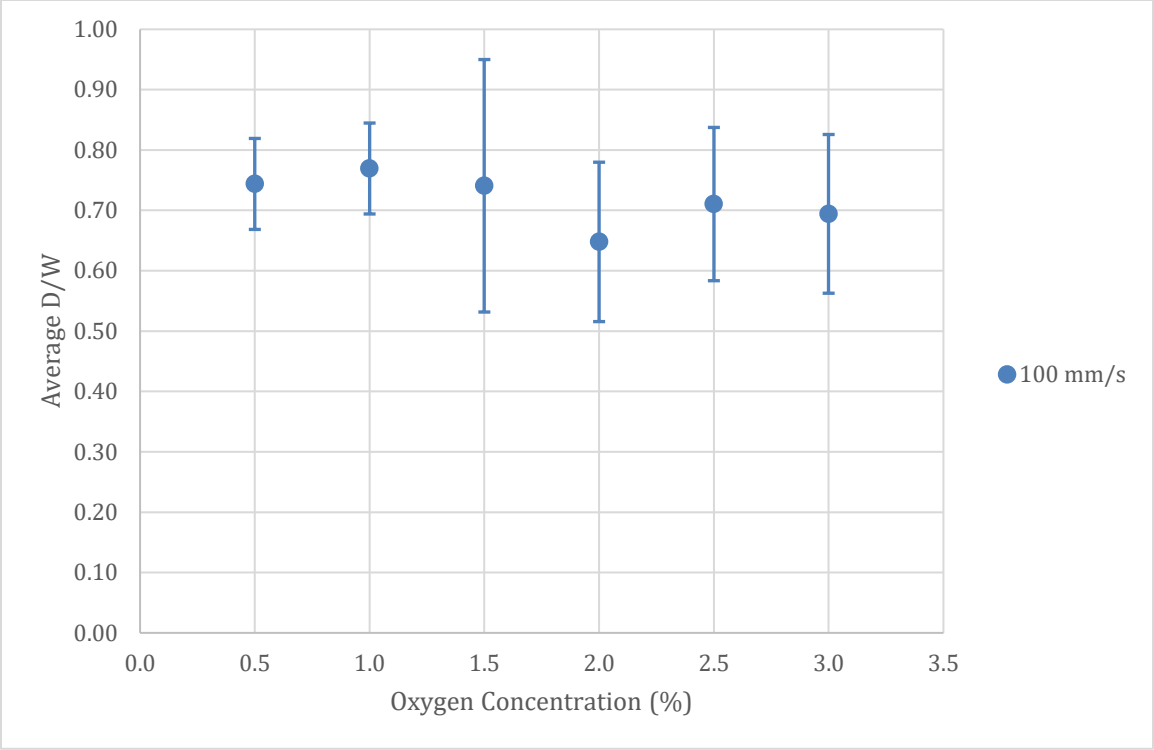

Figure 15. Average D/W vs. Oxygen, 100 mm/s Scan Speed, Standard Deviation

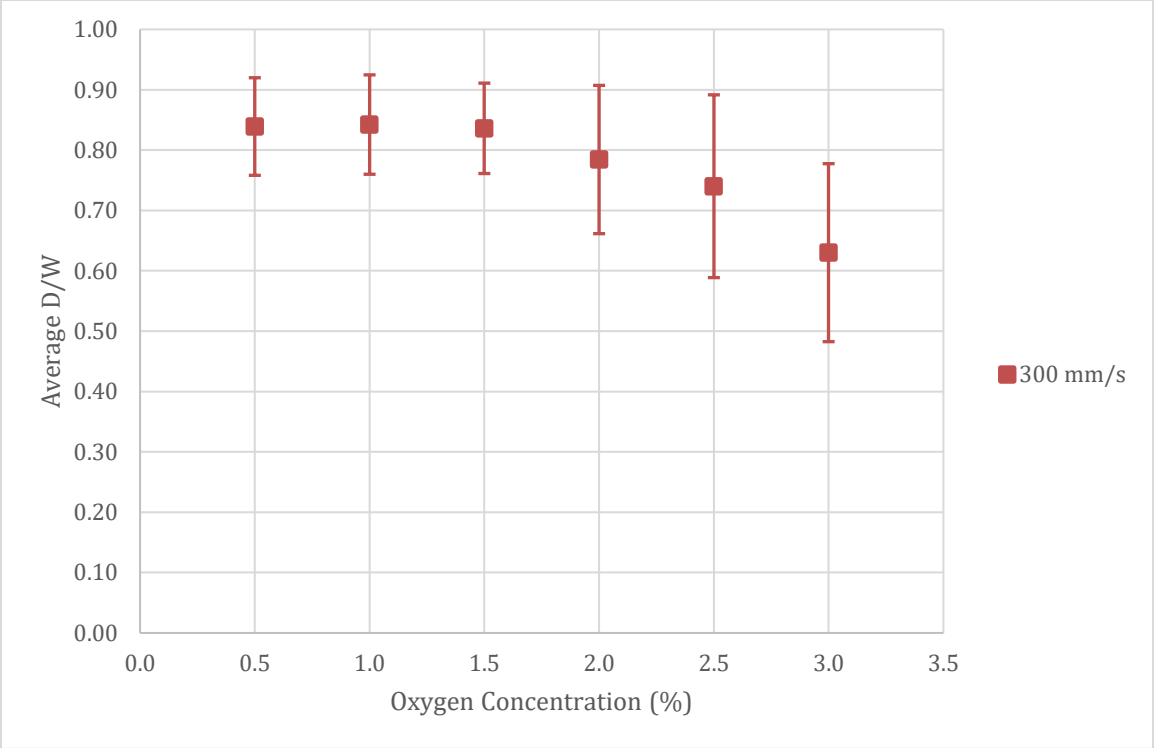

Figure 16. Average D/W vs. Oxygen, 300 mm/s Scan Speed, Standard Deviation

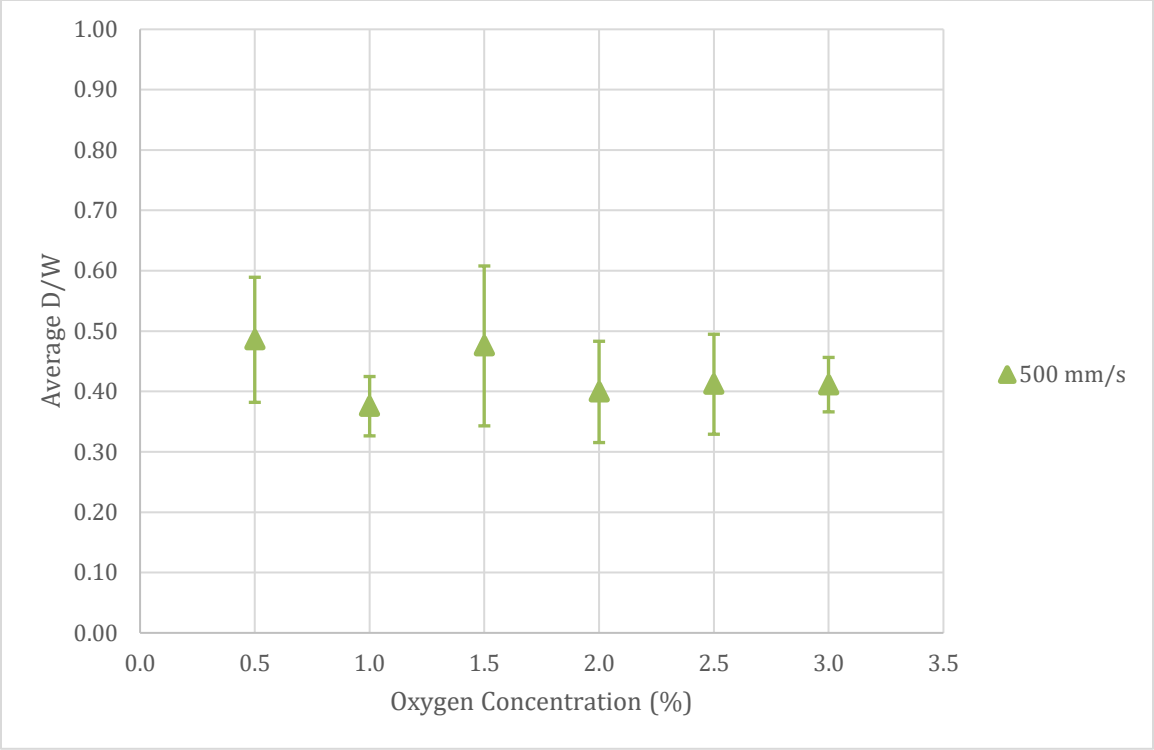

Figure 17. Average D/W vs. Oxygen, 500 mm/s Scan Speed, Standard Deviation

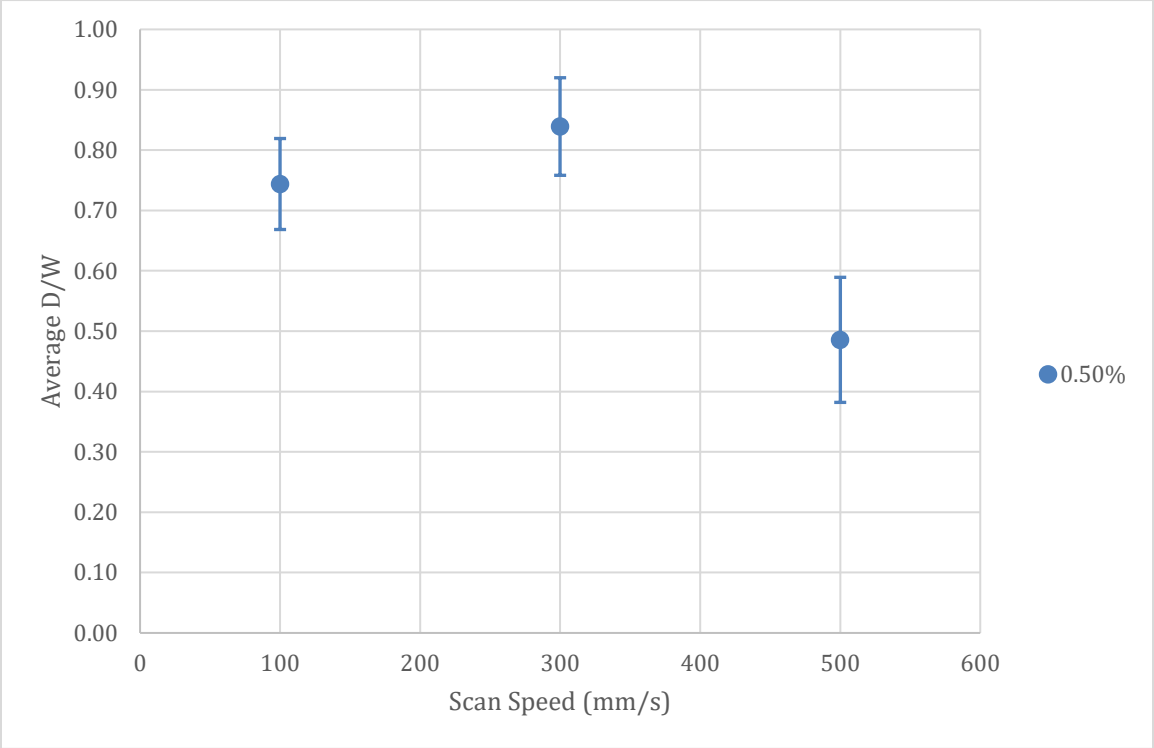

Figure 18. Average D/W vs. Scan Speed, 0.5% Oxygen, Standard Deviation

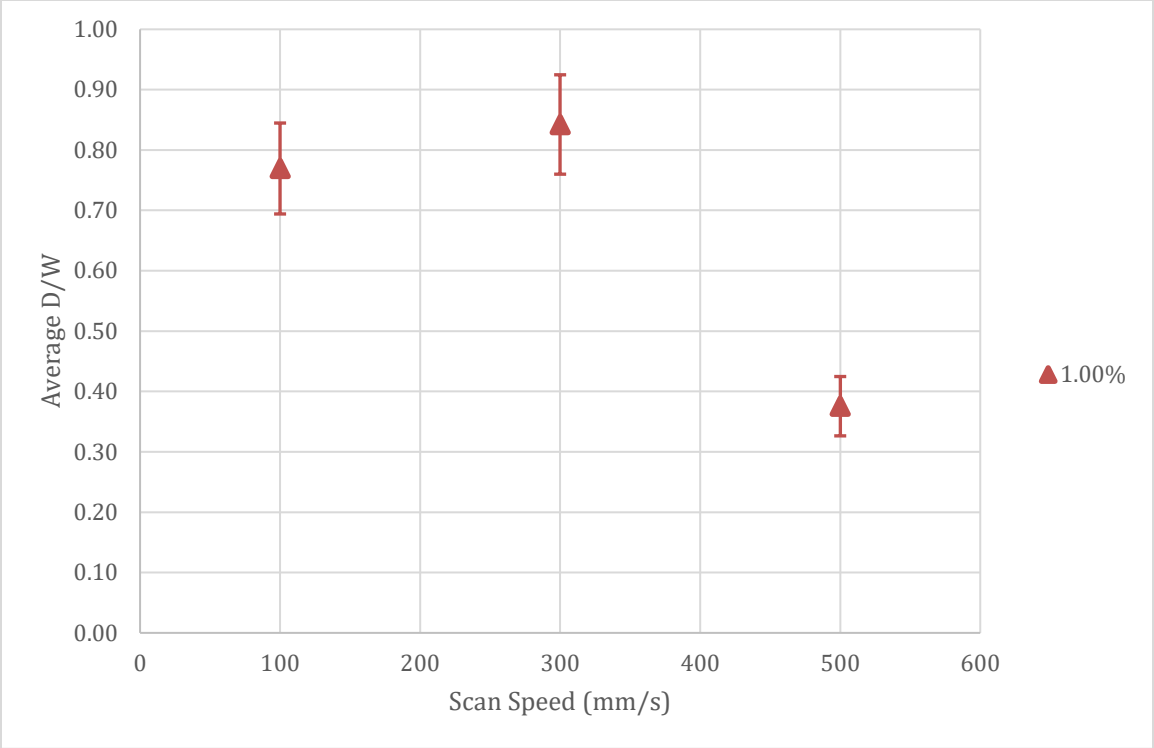

Figure 19. Average D/W vs. Scan Speed, 1.0% Oxygen, Standard Deviation

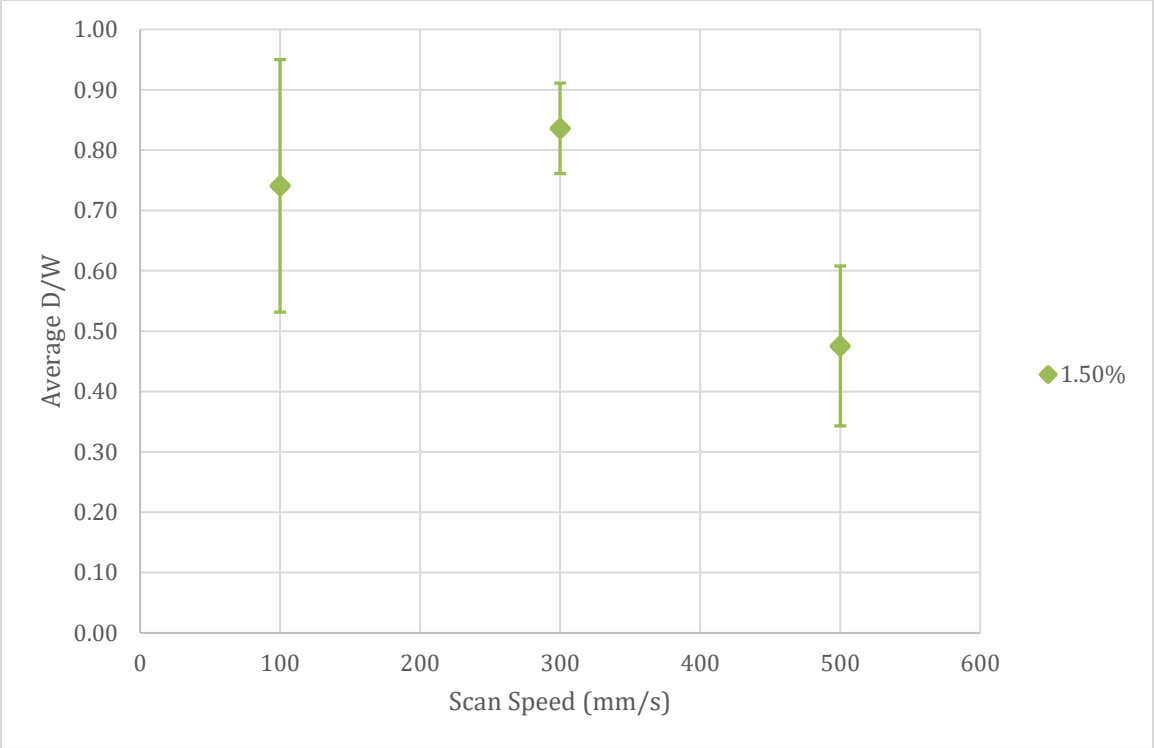

Figure 20. Average D/W vs. Scan Speed, 1.5% Oxygen, Standard Deviation

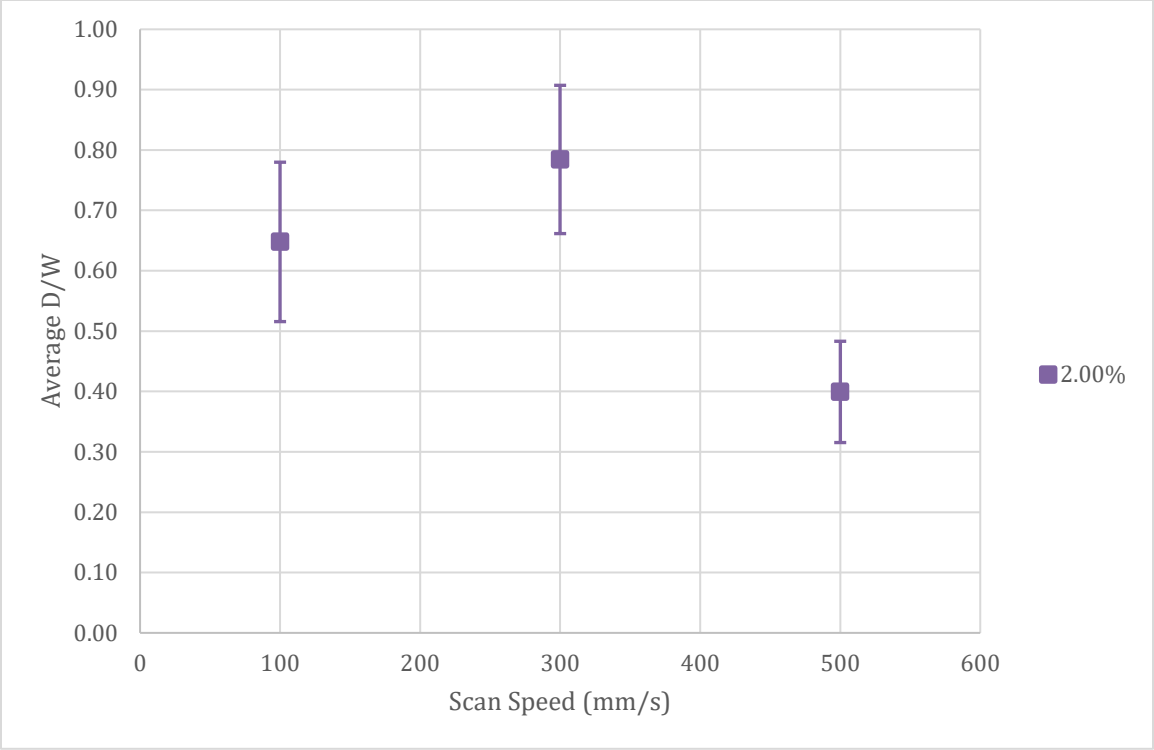

Figure 21. Average D/W vs. Scan Speed, 2.0% Oxygen, Standard Deviation

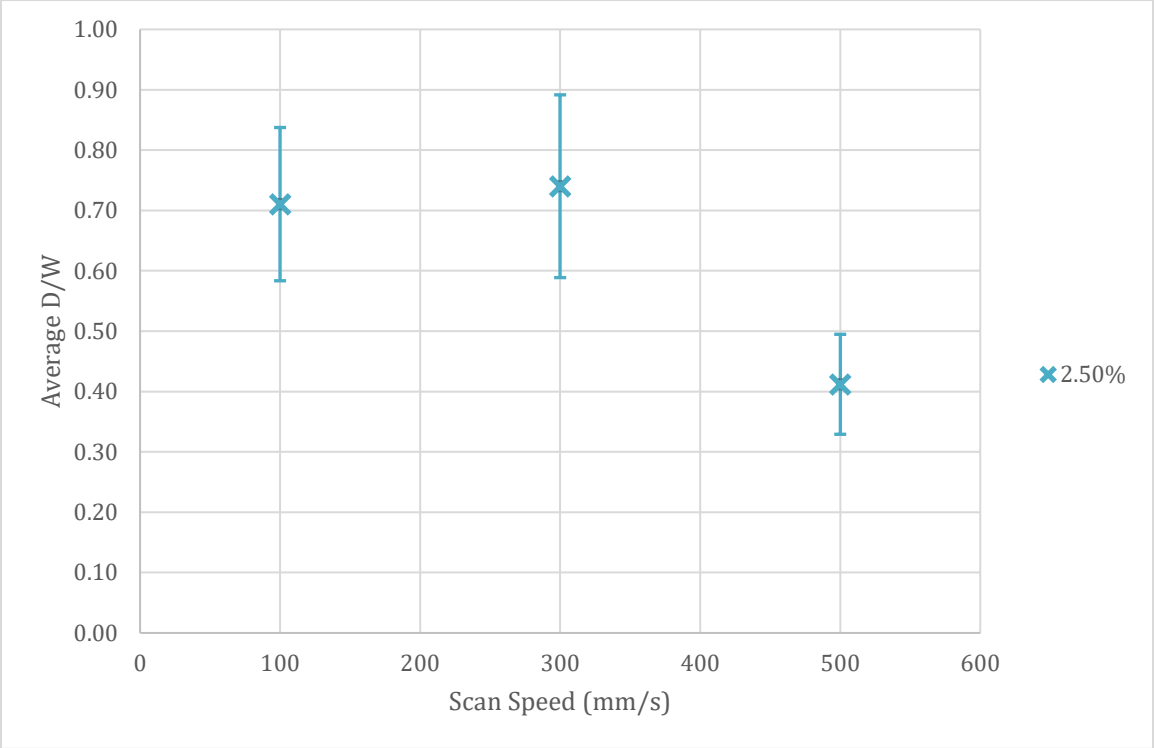

Figure 22. Average D/W vs. Scan Speed, 2.5% Oxygen, Standard Deviation

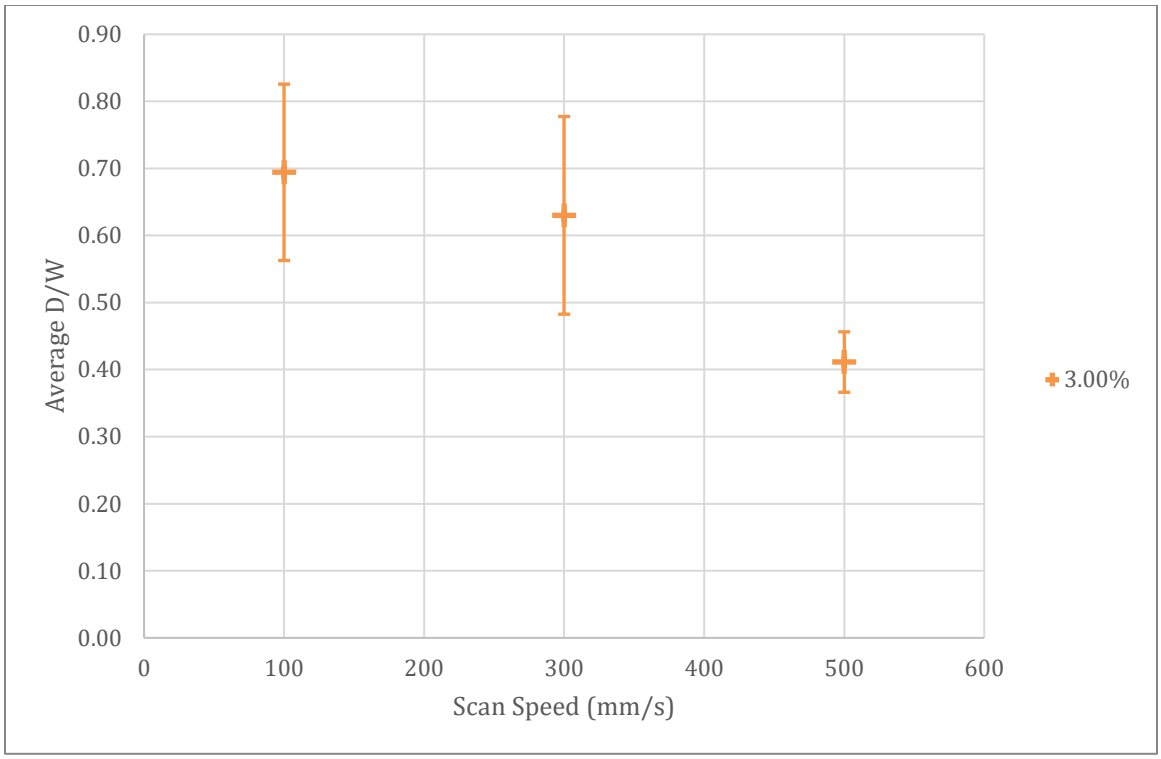

Figure 23. Average D/W vs. Scan Speed, 3.0% Oxygen, Standard Deviation

APPENDIX B

Table 8. Depths, Widths, and Ratios for First Set, Samples 1-4

Trial	Laser Power (W)	Scan Speed (mm/s)	Depth (μm)	Width (μm)	D/W Ratio
1.1	50	50	N/A	N/A	#VALUE!
			N/A	N/A	#VALUE!
			N/A	N/A	#VALUE!
			N/A	N/A	#VALUE!
1.2	50	500	N/A	N/A	#VALUE!
			N/A	N/A	#VALUE!
			N/A	N/A	#VALUE!
			N/A	N/A	#VALUE!
1.3	400	50	N/A	N/A	#VALUE!
			N/A	N/A	#VALUE!
			N/A	N/A	#VALUE!
			N/A	N/A	#VALUE!
1.4	400	500	239.24	194.03	1.23
			235.17	233.14	1.01
			232.63	210.79	1.10
			240.25	209.78	1.15

Table 9. Depths, Widths, and Ratios for Second Set, Samples 1-4

Trial	Laser Power (W)	Scan Speed (mm/s)	Depth (µm)	Width (µm)	D/W Ratio
2.1	50	50	N/A	N/A	#VALUE!
			N/A	N/A	#VALUE!
			N/A	N/A	#VALUE!
			N/A	N/A	#VALUE!
2.2	50	500	N/A	N/A	#VALUE!
			N/A	N/A	#VALUE!
			N/A	N/A	#VALUE!
			N/A	N/A	#VALUE!
2.3	400	50	220.44	403.30	0.55
			212.32	398.73	0.53
			215.87	417.02	0.52
			N/A	N/A	N/A
2.4	400	500	114.79	230.60	0.50
			118.35	302.73	0.39
			117.33	269.71	0.44
			113.27	257.02	0.44

Table 10. Depths, Widths, and Ratios for Third Set, Samples 1-3

Trial	Oxygen Concentration (%)	Scan Speed (mm/s)	Bead	Depth (μm)	Width (μm)	D/W Ratio
3.1	0.5	100	1	277.33	462.22	0.60
			2	345.40	404.32	0.85
			3	333.21	402.79	0.83
			4	304.25	427.66	0.71
			5	292.57	418.03	0.70
			6	326.10	439.37	0.74
			7	327.11	413.46	0.79
			8	314.92	434.79	0.72
3.2	0.5	300	1	363.71	399.79	0.91
			2	376.47	409.99	0.92
			3	292.66	440.50	0.66
			4	366.86	405.44	0.90
			5	319.13	412.56	0.77
			6	340.37	410.01	0.83
			7	344.58	414.64	0.83
			8	359.34	408.10	0.88
3.3	0.5	500	1	99.05	257.03	0.39
			2	90.92	249.90	0.36
			3	145.78	260.07	0.56
			4	148.32	294.10	0.50
			5	201.15	305.78	0.66
			6	109.71	272.25	0.40
			7	114.29	278.38	0.41
			8	164.07	273.78	0.60

Table 11. Depths, Widths, and Ratios for Third Set, Samples 4-6

Trial	Oxygen Concentration (%)	Scan Speed (mm/s)	Bead	Depth (μm)	Width (μm)	D/W Ratio
3.4	1.0	100	1	358.60	422.60	0.85
			2	354.58	400.29	0.89
			3	271.24	425.14	0.64
			4	320.65	421.21	0.76
			5	341.84	416.00	0.82
			6	322.54	421.59	0.77
			7	302.73	418.03	0.72
			8	298.16	419.56	0.71
3.5	1.0	300	1	324.06	413.46	0.78
			2	335.75	414.48	0.81
			3	342.86	416.00	0.82
			4	328.63	410.41	0.80
			5	324.06	430.73	0.75
			6	350.98	403.30	0.87
			7	351.49	409.40	0.86
			8	408.89	393.65	1.04
3.6	1.0	500	1	101.59	275.81	0.37
			2	125.46	293.59	0.43
			3	93.97	302.22	0.31
			4	102.60	284.95	0.36
			5	112.76	265.65	0.42
			6	94.48	289.52	0.33
			7	95.49	284.44	0.34
			8	125.46	277.84	0.45

Table 12. Depths, Widths, and Ratios for Third Set, Samples 7-9

Trial	Oxygen Concentration (%)	Scan Speed (mm/s)	Bead	Depth (µm)	Width (µm)	D/W Ratio
3.7	1.5	100	1	356.59	413.52	0.86
			2	306.32	424.26	0.72
			3	292.58	405.36	0.72
			4	424.15	389.09	1.09
			5	353.03	403.83	0.87
			6	160.51	355.58	0.45
			7	320.52	404.34	0.79
			8	152.90	371.31	0.41
3.8	1.5	300	1	314.42	423.11	0.74
			2	353.02	419.56	0.84
			3	340.83	409.90	0.83
			4	355.56	412.45	0.86
			5	306.29	427.69	0.72
			6	357.59	432.26	0.83
			7	380.95	422.60	0.90
			8	385.53	399.25	0.97
3.9	1.5	500	1	180.83	297.14	0.61
			2	171.18	286.48	0.60
			3	95.49	372.83	0.26
			4	154.92	271.24	0.57
			5	180.32	291.56	0.62
			6	106.67	289.02	0.37
			7	96.00	279.37	0.34
			8	126.48	288.00	0.44

Table 13. Depths, Widths, and Ratios for Third Set, Samples 10-12

Trial	Oxygen Concentration (%)	Scan Speed (mm/s)	Depth (µm)	Width (µm)	Width	D/W Ratio
3.10	2.0	100	1	267.68	429.73	0.62
			2	293.59	417.02	0.70
			3	358.60	414.99	0.86
			4	318.99	433.27	0.74
			5	320.01	420.09	0.76
			6	206.74	420.07	0.49
			7	201.15	415.49	0.48
			8	215.37	416.52	0.52
3.11	2.0	300	1	257.02	428.70	0.60
			2	303.75	428.70	0.71
			3	334.22	403.30	0.83
			4	325.59	406.35	0.80
			5	326.10	423.11	0.77
			6	370.79	389.08	0.95
			7	383.49	398.22	0.96
			8	274.79	422.60	0.65
3.12	2.0	500	1	119.87	272.76	0.44
			2	96.00	293.59	0.33
			3	164.07	292.57	0.56
			4	115.30	276.83	0.42
			5	119.37	276.32	0.43
			6	95.49	318.99	0.30
			7	94.48	322.54	0.29
			8	126.99	298.16	0.43

Table 14. Depths, Widths, and Ratios for Third Set, Samples 13-15

Trial	Oxygen Concentration (%)	Scan Speed (mm/s)	Bead	Depth (µm)	Width (µm)	D/W Ratio
3.13	2.5	100	1	339.31	419.56	0.81
			2	331.18	412.95	0.80
			3	230.61	429.74	0.54
			4	193.02	413.98	0.47
			5	345.91	425.15	0.81
			6	317.97	417.02	0.76
			7	297.15	426.67	0.70
			8	326.10	408.89	0.80
3.14	2.5	300	1	231.63	429.72	0.54
			2	299.17	449.52	0.67
			3	331.69	418.06	0.79
			4	298.67	416.00	0.72
			5	356.57	397.21	0.90
			6	224.51	445.98	0.50
			7	358.60	406.35	0.88
			8	370.29	401.78	0.92
3.15	2.5	500	1	142.22	294.60	0.48
			2	122.42	266.17	0.46
			3	128.51	307.30	0.42
			4	91.43	307.81	0.30
			5	146.29	258.04	0.57
			6	103.62	286.48	0.36
			7	104.13	274.79	0.38
			8	105.65	320.00	0.33

Table 15. Depths, Widths, and Ratios for Third Set, Samples 16-18

Trial	Oxygen Concentration (%)	Scan Speed (mm/s)	Bead	Depth (µm)	Width (µm)	D/W Ratio
3.16	3.0	100	1	342.35	406.86	0.84
			2	182.86	407.87	0.45
			3	279.87	442.41	0.63
			4	350.48	400.76	0.87
			5	310.35	409.91	0.76
			6	315.94	424.13	0.74
			7	291.56	432.27	0.67
			8	253.56	436.83	0.58
3.17	3.0	300	1	335.75	415.49	0.81
			2	278.35	427.68	0.65
			3	257.52	454.10	0.57
			4	188.95	406.35	0.46
			5	271.24	434.29	0.62
			6	350.98	419.05	0.84
			7	148.83	390.10	0.38
			8	298.67	423.11	0.71
3.18	3.0	500	1	120.38	266.67	0.45
			2	101.59	296.65	0.34
			3	95.49	263.64	0.36
			4	119.37	255.49	0.47
			5	107.18	289.03	0.37
			6	102.61	253.97	0.40
			7	126.98	277.34	0.46
			8	107.18	246.86	0.43

APPENDIX C

A sample code for a trial of eight beads at a scan speed of 100 mm/s is shown below.

File: BOP_100mm_s_eight.dbd

Unit: inch

Start_List

LaserOnDelay 0

LaserOffDelay 120

JumpSpeed 30.000

MarkSpeed 3.937

JumpDelay 500

MarkDelay 500

StepPeriod 100

jump_abs -0.2800 0.2800

weld_for 0.000000

mark_abs -0.2800 -0.2800

jump_abs -0.2000 0.2800

weld_for 0.000000

mark_abs -0.2000 -0.2800

jump_abs -0.1200 0.2800

weld_for 0.000000

mark_abs -0.1200 -0.2800

jump_abs -0.0400 0.2800

weld_for 0.000000

mark_abs -0.0400 -0.2800

jump_abs 0.0400 0.2800

weld_for 0.000000

mark_abs 0.0400 -0.2800

jump_abs 0.1200 0.2800

weld_for 0.000000

mark_abs 0.1200 -0.2800

jump_abs 0.2000 0.2800

weld_for 0.000000

mark_abs 0.2000 -0.2800

jump_abs 0.2800 0.2800

weld_for 0.000000

mark_abs 0.2800 -0.2800

End_List